Department of Condensed Matter Physics

UNIVERSITÉ DE GENÈVE

Research report

Scanning tunneling spectroscopy

Applications of superconductivity

Specific heat of oxide superconductors

High pressure transport measurements

Correlated electron systems

Films and heterostructures

Electronic nanostructures

Crystal growth

2004

Introduction

Since 2001 the Condensed Matter Physics Department (DPMC) in Geneva has been the leading house of the National Center of Competence in Research (NCCR) MaNEP "Materials with Novel Electronic Properties". This center, with the University of Geneva as host institution and a broad Swiss network, focuses its activities on research and development of novel materials with promising electronic properties. The NCCR, which has been very successful in its first 4-year phase, has recently been renewed for a 4-year second phase allowing the further development of the research activities at the DPMC in the field of correlated electron systems.

The DPMC has a long tradition in the studies of metallic materials with unconventional properties. In the last decade the interest of the department has been focused mostly on the understanding and development of high temperature superconductors and more recently superconducting MgB_2 as well as several classes of key novel materials, including colossal magnetoresistance compounds and ferro/dielectric oxides. All these materials have low electronic densities and a physics dominated by electronic interactions. The DPMC in Geneva has long standing experience in producing high quality materials in the form of single crystals, thin films and heterostructures, and tapes. The department also has a large expertise in the study of the physical properties of such materials. Several top class high quality experimental set-ups allowing high magnetic field magnetotransport, transport under pressure, specific heat measurements, and recently optical spectroscopy are available. The department has also developed a large expertise in local probe systems. These include Scanning Tunneling Microscopy and Spectroscopy, STM/STS, and Atomic Force Microscopy, AFM, that allow the characterization and study of materials on a nanoscopic scale. This report represents the research carried out at the DPMC, regardless of the source of funds.

Organization of the department

Director: Jean-Marc Triscone

Faculty

Øystein Fischer
Tel. (022) 379 6270
e-mail: Oystein.Fischer@physics.unige.ch

Alain Junod
Tel. (022) 379 6204
e-mail: Alain.Junod@physics.unige.ch

René Flükiger
Tel. (022) 379 6240
e-mail: Rene.Flukiger@physics.unige.ch

Dirk van der Marel
Tel. (022) 379 6234
e-mail: Dirk.VanDerMarel@physics.unige.ch

Thierry Giamarchi
Tel. (022) 379 6363
e-mail: Thierry.Giamarchi@physics.unige.ch

Jean-Marc Triscone
Tel. (022) 379 6827
e-mail: Jean-Marc.Triscone@physics.unige.ch

Secretariat

Elisabeth Jeantin, Nicole Nguyen, Fabienne Piguet

Department facilities

Computing Service: Ivan Maggio-Aprile
Helium: Gregory Manfrini and Spiros Zanos
Electronics: Patrick Magnin, Laurent Stark
Teaching support: Charly Burgisser, Vincenzo Fontana, Lionel Windels

University of Geneva
Department of Condensed Matter Physics
24 quai Ernest-Ansermet
1211 Geneva 4
Switzerland
Phone: +41 22 379 6511 / 6224 / 6264
Fax: +41 22 379 6869
Web site: http://dpmc.unige.ch

The Fischer group

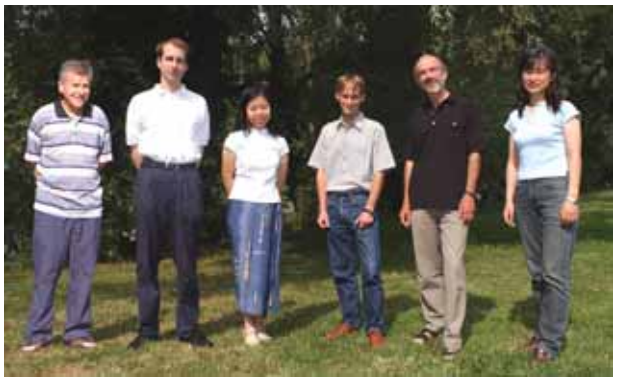

The Junod group

The Flükiger group

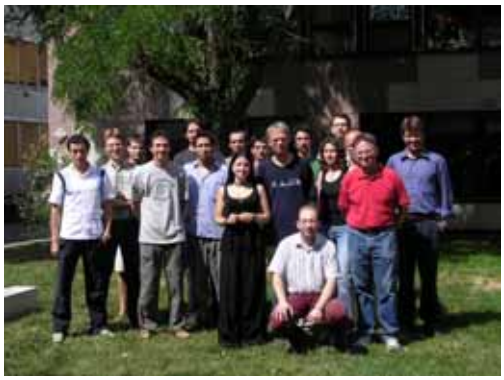

The van der Marel group

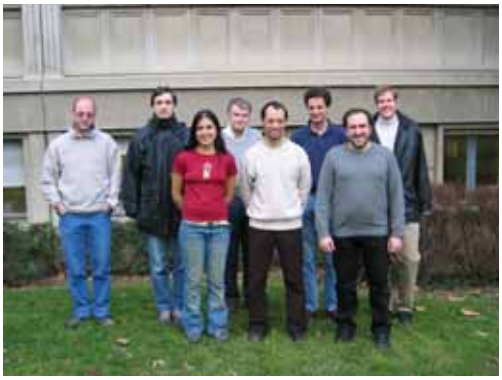

The Giamarchi group

The Triscone group

Technical staff

Secretariat

Research groups

Nanoscopic studies of superconductors and other interacting electron systems

Professor	Øystein FISCHER
MER	Michel DECROUX, Alfred MANUEL
Postdocs	Louis ANTOGNAZZA, Edmond KOLLER, Olivier KUFFER, Martin KUGLER, Ivan MAGGIO-APRILE, Sivaperumal UTHAYAKUMAR[1]; FASANO Yanina[2]
PhD students	Cédric DUBOIS, Nathan JENKINS, Pierre LEGENDRE, Giorgio LEVY DI CASTRO, Alexander PETROVIC, Alexandre PIRIOU, Silvia SEIRO, Matthieu THERASSE, Emmanuel TREBOUX
Visiting Research Fellow	Christian HESS[3]
Electronics Engineer	Laurent STARK
Technicians	Paul-Emile BISSON, Jean-Gabriel BOSCH, Géraldine CRAVOTTO

[1]until 30.09.2004, [2]from 01.02.2004, [3]until 31.12.2004,

Applications of superconductivity

Professor	René FLÜKIGER
Postdocs	Nicholas CLAYTON, Enrico GIANNINI, Bernard REVAZ, Carmine SENATORE, Hongli SUO[1], Grégoire WITZ
Visiting Research Fellow	GLADYSHEVSKII Roman[2],
PhD students	Nicolas MUSOLINO, QU Timing[3], Michael SCHINDL[4]
Technicians	Patrick CERUTTI, Simon HUGI

[1]until 31.03.04; [2] from 01.12.04; [3]from 01.08.04, [4]until 31.08.04

Theory of Condensed Matter

Professor	Thierry GIAMARCHI
MER	Thomas JARLBORG
Postdocs	Christophe BERTHOD, Carlos BOLECH GRET, Anibal IUCCI[1], Alejandro KOLTON, Alberto ROSSO[2]
Visiting Research Fellow	Lara BENFATTO[3], Claudia PEÇA[4]
PhD students	Gladys LEON SUROS[5]

[1]from 01.09.04; [2]until 30.09.04, [3]until 30.11.04; [4]until 31.10.04, [5]from 01.09.04

Fundamental excitations of correlated matter

Professor	Dirk van der MAREL
Postdocs	Alexey KUZMENKO, Alexander BRINKMAN[1]
PhD students	Fabrizio CARBONE, Violeta GURITANU, Erik van HEUMEN Hajo MOLEGRAAF[2], Riccardo TEDIOSI, Dook van MECHELEN[3], Jérémie TEYSSIER[4]
Technician	Cornelis BOS, Mehdi BRANDT[5]

[1]from 01.04.04; [2]until 31.10.04; [3]from 01.11.04; [4]from 01.10.04; [5]from 01.03.04

Specific heat and magnetocaloric effect of metals and superconductors

Professor	Alain JUNOD
Postdoc	Satoko ABE, Tomasz PLACKOWSKI[1], Rolf LORTZ, Ulrich TUTSCH, Yuxing WANG
Technician	Aldo NAULA

[1]from 01.11.04

Growth and electronic properties of unconventional metals and oxides

Professor	Jean-Marc TRISCONE
MER	Didier JACCARD
Postdocs	Matthew DAWBER, Stefano GARIGLIO, Alexander HOLMES[1], Daniel MATTHEY, Pablo PEDRAZZINI[2], Kei TAKAHASHI
PhD students	Alexandre GUILLER, Céline LICHTENSTEIGER, Patrycja PARUCH, Nicolas REYREN[3], Anna-Sabina RUETSCHI[4], Nicolas STUCKI
Technicians	Renald CARTONI, Daniel CHABLAIX

[1]until 31.10.04; [2]from 01.09.04; [3]from 01.11.04;[4]from 01.05.04

Nanoscopic studies of superconductors and other interacting electron systems

Øystein FISCHER

Research summary: This group investigates superconductors by scanning tunnelling spectroscopy. Such measurements have already demonstrated the non BCS behaviour of high temperature superconductors. This is seen both in the temperature and doping dependence of spectra as well as by the behaviour of the vortex core spectra. In this project we here report on first STS investigations of the three layer compound $Bi_2Sr_2Ca_2Cu_3O_{10}$ as well as on the detailed behaviour of the vortex core spectra in the two layer compound $Bi_2Sr_2CaCu_2O_8$. We have started new studies of the compound $YBa_2Cu_4O_8$. The motivation is here that this compound is stoichiometric and therefore expected to be less prone to gap inhomogeneities. This programme also incorporates studies of other superconductors. This year we have continued the studies of MgB_2 by investigating the effect of doping with Al and C. Finally we have developed a new x-y table incorporated into the STM. This is a completely original design which shall allow us to increase the scan range of STM considerably. We have continued the instrumental development in view of scanning tunnelling potentiometry investigations of thin film manganites. A new effort to produce thin superconducting films by pulsed lased deposition has concentrated on $La_{2-x}Sr_xCuO_4$. The focus of this work is on the surface properties and the possibility of carrying our surface sensitive measurements on such films. Finally we have extended our research on the use of thin YBCO films in fault current limiters.

Scanning Tunneling Spectroscopy on $Bi_2Sr_2Ca_2Cu_3O_{10}$

$Bi_2Sr_2Ca_2Cu_3O_{10}$ (Bi2223) attracted strong interest due to its high critical temperature Tc(max)=111K and its potential for applications. However, the difficulty in synthesizing large sized single-phase crystals significantly impeded the study of fundamental properties. Very recently the effort in developing new crystal growth processes was rewarded by a successful production of homogeneous high quality Bi2223 single crystals (see section B of this report) allowing scanning tunnelling spectroscopy (STS). The study of the intrinsic superconducting properties of this trilayer compound is of crucial importance for the determination of the generic features and behaviors of Bismuth based cuprates and more generally in the quest of the understanding of high-Tc superconductivity.

With this aim we recently succeeded in performing the first STS experiments on Bi2223 single crystals [1]. We studied various high quality crystals annealed under different conditions. In one case, for Tc=109K and a transition width of only 1K, we obtained an extremely homogeneous sample with Δ_p=60meV over at least 50nm as shown in Fig.1. In another case, the respective parameters were Tc=111K and ΔTc=1.7K and yielded a slightly less homogeneous sample with Δ_p=45meV. The doping phase diagram Tc(*p*) of Bi2223 has yet not been determined in detail. However, by analysing the slope of the background conductance and comparing it to the systematic variation as a function of doping observed in Bi2212, we found a way to determine the doping level of the investigated Bi2223 samples (See Fig.1). The increase of the gap magnitude with decreasing doping level is furthermore consistent with what has previously been observed on Bi2212 and Bi2201. It thus appears that the sample with Δ_p=60meV is underdoped,

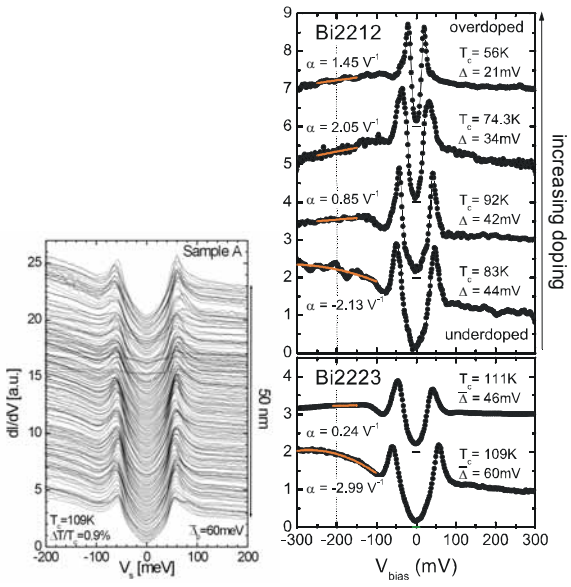

Figure 1: Left: Spectral trace of 201 spectra acquired at T=1.8K along a 50nm line on Bi2223. The gap distribution width is remarkably small σ =3 meV. I = 0.6nA, Vs = 0.3V. Right: Comparison of the LDOS doping dependence between Bi2212 [2] and Bi2223. All spectra have been normalized to the background conductance at Vs=300meV and shifted vertically for clarity. α is the slope of the background fit at Vs=-200meV. The Bi2223 panel shows the average spectra of traces obtained on the samples mentioned in the text.

whereas the one with Δ_p=45meV is close to optimal doping. Investigating the spatial variation of the spectra on surfaces which are less homogeneous revealed, that the spectra evolve similarly to Bi2212 when moving the tip from a superconducting region to a degraded zone: the

intensity of the peaks decreases, the gap magnitude increases and the spectra gradually evolve to a pseudogap-like signature which finally resumes into a semiconductor-like line-shape. This behavior is typical for regions where the oxygen doping level is locally being reduced. On the other hand, we also observed regions where the superconducting coherence is lost without an increase of the gap magnitude. Here the resulting pseudogap shows the samemagnitude as the superconducting gap measured close-by. This demonstrates that there is an effect different from a varying oxygen concentration that is at the origin of the coherence loss. This is also consistent with results found in Bi2212.

Finally, based on the scaling between the pseudogap temperature T* and the gap magnitude which we determined in previous work, we estimate T* to be about room temperature for Bi2223. To confirm this estimate, the temperature dependence of Bi2223 is currently under investigation. The objective of future work, is also the observation of vortex cores in Bi2223. In this compound, the gap magnitude being larger than in Bi2212, detailed core spectroscopy might reveal important clues with respect to the localized core-states which have been observed in Bi2212.

Scanning Tunneling Spectroscopy of the vortexcores in $Bi_2Sr_2Ca_1Cu_2O_8$

We have also carried out a detailed study of the local density of states spatial modulations that exist in the vortex core of $Bi_2Sr_2CaCu_2O_8$ [2] This part of the project was financed by another source but since it is directly related to the work on Bi2223 and YBCO124 we report it here. We observed vortex-core states located at ±6meV (Fig. 2a) and the existence of a square pattern, extending the results obtained by Hoffman et al. The Fourier transform reveals four peaks (q_1) corresponding to a $4.3a_0$ - square modulation (Fig. 2b). We demonstrated that the amplitude of the vortex core-states reflects directly the four-fold modulation observed in the vortex core. In previous work we showed that the energy of the

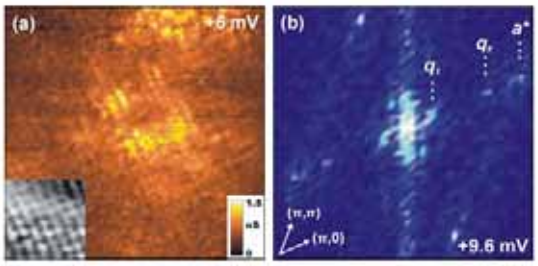

Fig. 2. (a) Conductance map of the core-state in a vortex core at V=6meV, H=6T, T=1.8K. (b) Fourier Transform of the real space map taken at V=+9.6mV evidencing peaks (q_1) corresponding to a four-fold pattern with period $4.3a_0$.

Vortex core-states scales with the superconducting gap magnitude Δ_p measured just outside the core. Combining these two observations provides a connection between the superconducting state and the four-fold electronic modulation in the vortex core. Furthermore this modulation does not disperse in energy suggesting a common origin to the one observed in the pseudogap phase by Vershinin et al. [8].

Scanning Tunneling Spectroscopy on $YBa_2Cu_4O_8$ (YBCO124)

Scanning tunneling spectroscopy (STS) in the paramount $YBa_2Cu_3O_7$ (YBCO123) compound provided key information on the superconducting microscopic electronic properties of high Tc materials [1]. Recently, a considerable amount of studies pointed out the need for understanding the role played by inhomogeneities in the observed electronic properties [2]. The study of the related compound YBCO124, stoechiometric in oxygen, brings the possibility to avoid the effects arising from inhomogeneities in the electronic doping. On the other hand, it allows in principle to address the relation between superconducting and pseudogap phases since it is considered as intrinsically underdoped. However, because of the complexity in obtaining high-quality YBCO124 single crystals, local electronic measurements are lacking.

This motivated us to perform the first STS studies in as-grown surfaces of YBCO124 single crystals. The observed systematic reduction of the tunnelling conductance at low bias voltage reveals gapped spectra. As an example, Fig.3(a) shows a set of spectra acquired at 4.2 K along a 10 nm line with a tunnel junction resistance of 1 GΩ. Coherence peaks are not developed as in YBCO123, inhibiting a precise determination of the gap value. A preliminary analysis of the

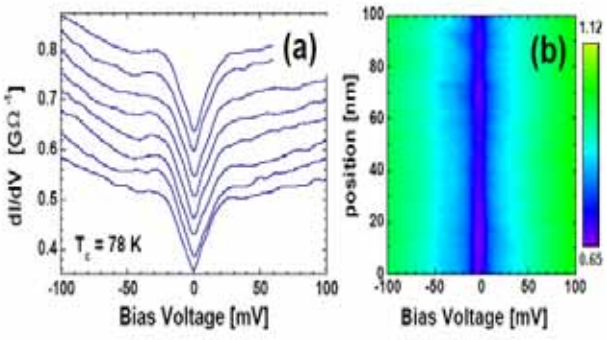

Fig. 3. Tunneling spectroscopy on YBCO124 at 4.2 K (a) Spectra along a 10 nm trace (curves are shifted for clarity). (b) Conductance color-level plot along a 100 nm trace.

conductance data gives an estimation of the gap of 25 ± 10 meV. The shape of the spectra suggest that we are observing the pseudogap rather than the superconducting gap. This would imply that the superonducting coherence is lost at the surface. Whether this is intrinsic or extrinsi remains to be seen. The color-level plot of conductance spectra along a 100 nm trace shown in Fig. 3(b) uncovers the spatial homogeneity of the crystals at the micrometric scale. A thorough analysis is underway.

Scanning Tunneling Spectroscopy on MgB_2

Two-band superconductivity in MgB_2 is now well established [3,4]. For pure MgB_2 the π band is nearly isotropic with a superconducting gap of 2.2 meV, while the σ band is highly two-dimensional with a gap of 7.2 meV. Our previous STS measurements show that the coherence length associated to the π band (roughly 50 nm) is much larger than the value estimated from H_{C2}, suggesting different coherence lengths in the two bands [5]. With pure MgB_2 now being relatively well understood, the next step is to try and increase the interband coupling (for example, by introducing dopants) which should lead to the properties of the two bands approaching each other and possibly merging completely (known as the dirty limit). Research in this group during 2004 has continued on Aluminium-doped MgB_2 and has begun on Carbon-doped MgB2.
Figure 4 shows measurements of Al-doped MgB2 presenting a homogeneous surface and a π gap of ~2.7 meV, compared to that of 2.2 meV for pure MgB_2. Further measurements (not shown) indicate a reduction in the π band

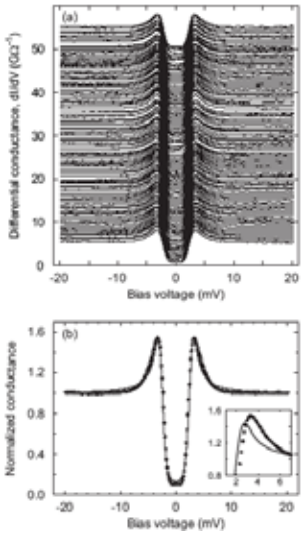

Figure 4 : Tunneling spectra of Al-doped MgB_2 at 300 mK. (a) Spectra along a 100 nm line (offset for clarity). (b) The points depict an averaging of the spectra shown in (a) whereas the line is a BCS s-wave fit of the spectra. The inset shows a comparison between Al-doped and pure MgB_2 spectra in the vicinity of a coherence peak.

coherence length from roughly 50 nm to 25 nm, consistent with the two-band nature of MgB_2.

New Instrumentation for Nanolithography

One limitation of our approach to STM/STS is the limited field of view (1-4 mm2) ones the sample cooled. We have therefore developed a corse x-y large scan motion. This is done generalizing the one dimensional slip-stick motion to 3 dimensions.

Plugged in directly at the extremity of the scanner tube, it consists of two inertially driven carriages mounted perpendicularly on top of each other with the tip fixed at the bottom. The stick and slip motion is powered by the scanner tube. With this configuration we succeed in avoiding any coupling between the x,y and z movement and thus perform scanning tunneling topography and spectroscopy on an entire sample surface. Its calibrated motion range is 6mm x 3mm in the horizontal plane. Two differential capacitive detectors allow for submicronic tip positioning precision (Fig. 5).

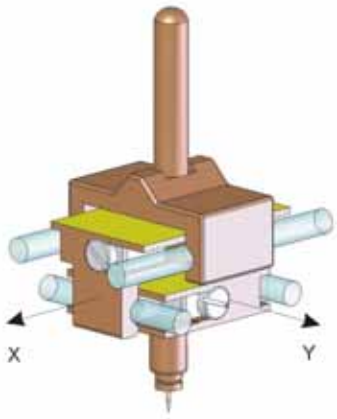

Figure 5 : XY-stage plug-in. The motion range is 6 mm along the x-axis and 3mm along the y-axis. The volume of the stage is 2.2 cm^3.

The xy-stage is currently mounted on a low temperature STM facility equipped with a 9T magnet and a large controllable temperature range. Its mechanical stability has been successfully demonstrated at micrometer scale by imaging a NanoGrid which consists of a 2-dimensional array with a square pitch of 160 nm coated with a thin layer of gold and at nanometer scale by achieving atomic resolution on HOPG.

To show that high quality tunneling spectroscopy can be achieved at low temperature, we demonstrated reproducible spectra taken on a $NbSe_2$ single crystal, as well as on MgB_2 as shown in Fig. 4.

STM/STS/STP on Manganites

The doped rare earth manganese oxides with perovskite structure, focus of this project, exhibit an extremely rich phase diagram as a function of composition, doping, temperature, pressure and magnetic field. The zoology of observed phases spans from charge/orbital ordered insulators to ferromagnetic metals, including even the astounding coexistence of magnetism and ferroelectricity. For certain doping values these compounds exhibit an insulator to metal transition triggered by the ordering of localized spins, either by cooling below the ferromagnetic critical temperature (T_c) or by the application of a magnetic field slightly above T_c. The huge decrease of resistance when increasing the magnetic field in the latter case is known as colossal magnetoresistance (CMR).

The CMR phenomenon is a subject of numerous theoretical studies. An increasing amount of them are in favour of a phase separation scenario, where the insulator-metal transition is percolative and associated to the intrinsic inhomogeneity of the materials [4]. Within this framework the proposed domain sizes range from nanometer to micrometer scale, depending on the physical mechanisms considered in the models [3]. Such a variety of length scales has indeed been observed by local probe techniques [4]. However, no experimental investigation published up to this date has provided a truly convincing answer to the problem. The reason for this lies in the difficulty to distinguish experimentally "intrinsic" electronic inhomogeneities from those arising from strain, variations in oxygen content, or surface contamination. Therefore, a careful and thorough study at the microscopic scale is mandatory to determine the existence, size, and dependence on thermodynamic variables of these domains, as well as their relation to the macroscopic CMR effect. Scanning tunnelling spectroscopy (STS) would be perfectly suited for this purpose since it provides atomic and nanoscopic imaging of electronic properties of the material.

Nevertheless, STS is extremely surface sensitive. Therefore two questions are raised: Whether surface measurements give an accurate picture of bulk properties, and whether observed electronic inhomogeneities are an intrinsic property of the material or rather a contamination/non-stoichiometry effect. To address the latter, high quality samples with flat, clean surfaces are needed. As a part of this project, thin films of the canonical manganite $La_{2/3}Ca_{1/3}MnO_3$ (LCMO) as well as $La_{1/4}Pr_{3/8}Ca_{3/8}MnO_3$ (LPCMO) are being grown in the laboratory by sputtering techniques. In Fig. 6, a STM topographic image, as well as a x-ray diffraction spectrum of a typical film of LCMO of 70 nm thickness is shown.

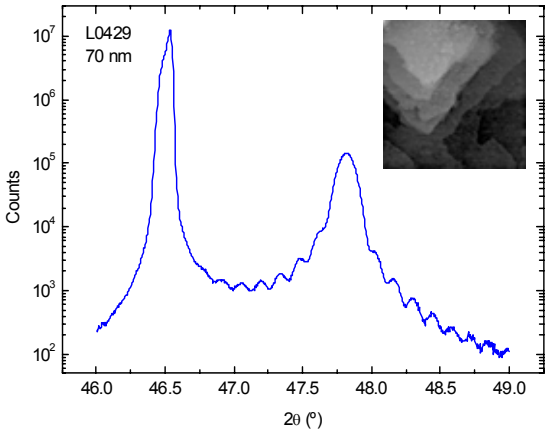

Fig. 6. Typical x-ray diffractogram around the 002 peak of an LCMO 70nm thick film. On the left, the substrate peak is observed, while the film peak on the right exhibits multiple size-effect oscillations, attesting the homogeneity of the c cell parameter of the film as well as of the sample thickness. The insert shows a characteristic 200 x 200 nm^2 STM topographic image of the sample.

The question of surface sensitivity is approached by the implementation of another technique of the STS family, namely scanning tunnelling potentiometry (STP), where a current is applied along the sample and the local potential drop is measured with an atomically sharp tip [5]. Simultaneously, local conductance and topography features are recorded. In this way, the STP technique reveals not only surface but also bulk properties of the sample. Although the technique has been successfully employed to study the manganite problem at room temperature [6], a comprehensive study as a function of temperature and magnetic field is lacking. The Escalab system, where in-situ grown films have been studied, allows only room temperature, zero magnetic field studies. Therefore a new "clean" controllable temperature and magnetic field scanning tunnelling microscope (STM) was built during 2004, the Calypso.

The Calypso system shown in Fig. 7 is composed of a ^{4}He flow cryostat, a glove box for sample preparation, and a STM insert. The cryostat allows a working temperature range between 4.2 K and room temperature, and is furnished with a superconducting magnet

which supplies up to 6 T. This rests on sand-filled columns standing on an independent concrete block to isolate the cryostat from external vibrations. With the same purpose, vacuum connections are made through a vibration isolated block. To provide a clean environment for sample preparation and mounting, the STM insert can be placed in an inert atmosphere glove box. Inside the glove box, a built in-house furnace allows annealing under controlled atmosphere (oxygen, argon or vacuum) up to temperatures of 450°C. The rough approach of the STM tip is made inside the glove box, and the position of the tip is monitored by an optical system of camera and lenses, see insert c in Fig. 7. When this process has been completed the insert can be hermetically sealed in the glove box and transferred to the cryostat without surface contamination of the sample.

Fig. 7. The Calypso system with the glove box in front (center). (a) Detail of the annealing furnace. (b) Detail of the cryostat. (c) Tip-sample approach inside the glove box as seen with the optical system. (d) STM head.

The STM head is composed of two concentric piezoelectric tubes, which provide for the tip displacements along the three axis, the approach of the sample to the tip and the lateral tilting. The sample is mounted on an inertial slider moving along two parallel sapphire rails. The temperature monitoring and control are provided by a thermometer and a PID controlled heater glued to the slider.

The movement of the slider has been tested and optimized at room temperature and liquid nitrogen temperature, and the first STM images have been obtained at room temperature. A careful STM study to obtain information on the microscopic processes related to the metal-insulation transition and the CMR phenomenon is currently under way.

Fault current limiter

We are currently working on superconducting thin films based Fault Current Limiter (FCL). These devices limit the current in an electrical network during a short circuit. The FCL is a meander of Au/YBCO/CeO heterostructure on a 2" wafer. During this year we have produced several 5kW (340V, 16A) FCL using our particular design and have measured their behavior during AC test. Briefly, the meander is made of constrictions and of connecting paths; the aim of the constrictions is to homogeneize the distribution of the dissipated power along the meander at the beginning of the short circuit. In order to confirm the benefits of this design we have tested our wafer during AC short circuits starting at different fault angle ϕ (i.e. different voltages). For instance, for a voltage of 150V, i.e. at 45% of U_{max}, there are dissipative zones in each of the 8 lines. The effect of the constrictions is evident as for the same meander but without constrictions, only 3 to 4 lines would have switched.
One of the important characteristics of the FCL is the recovery time, i.e. the time needed, after the end of the short circuit, to switch back the FCL into the superconducting state. By injecting a small current in the FCL during and after the short circuit, we have measured the restoring time for short circuit lengths ranging from 20 to 65ms. For instance the restoring time of the lines is 600-700ms and 750-900ms for short circuit lengths of 45 and 65ms respectively.

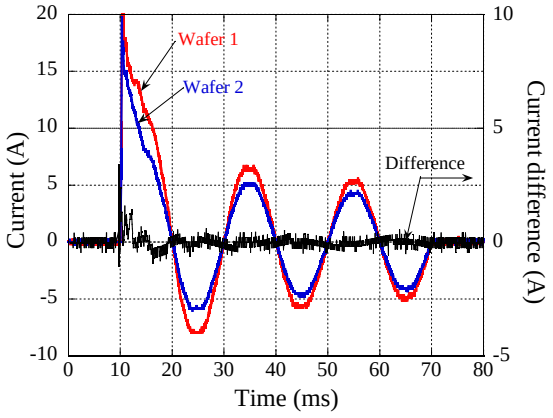

Fig. 8: Current in wafer 1 and 2, connected in parallel, during a 60ms short circuit. The other curve represents the difference between the currents in wafer 1 during the test in conjunction with wafer 2 and the individual test.

During this year we have also tested the behavior of two wafers connected in parallel. This 10kVA (340V, 32A) FCL has sustained short circuits up to 60ms (cf fig. 8). Our measurements show that the current in a

particular wafer is almost identical (difference of 300mA for a current of 5A) when this wafer is tested individually or when it is connected in parallel.
In order to have the possibility to grow large area thin films we have set up a new deposition chamber. In this system the three elements (Y,Ba,Cu) are evaporated simultaneously from three boats by Joule heating. We have calibrated all the deposition rate and already produced YBCO thin films on a smal (5x5mm) $SrTiO_3$ substrate. These films are superconducting and we are now optimizing the growth conditions.

Growth and properties of $La_{2-x}Sr_xCuO_4$

Following our previous studies on strain effect in $Nd_{1+x}Ba_{2-x}Cu_3O_{7+\delta}$, we have started to investigate another material, $La_{2-x}Sr_xCuO_4$ (LSCO), on which it has been claimed that strain could increase T_c [7]. Besides, ARPES measurments [8] led us to think that STM measurements should be possible also on this material (cf. STM part below).
On samples grown by magnetron sputtering, we have observed a large T_{co} variation (from 5 K to 33K) with deposition pressure, for films with a constant thickness (35 nm) and quality (inset fig. 9). This is likely to be due to a change in the stochiometry during transfer.

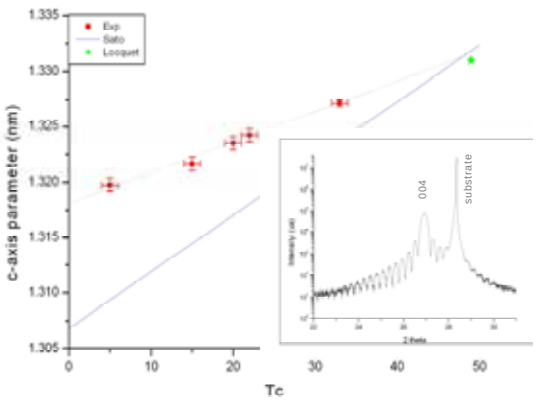

Fig. 9 : c-axis parameter vs T_c. Inset : Finite size effect around 004 for a film with T_c = 33 K.

In fact, a decrease in Sr content is known to change the c-axis as it lowers T_c [9] (fig. 10). In our case, a c-axis variation has been observed too, but less than expected (fig. 9). The loss of T_c could then be due to a lack of both Sr and Cu, copper deficiency being known to lower T_c dramatically without changing the c-axis. Actually, many authors use targets with excess of CuO in sputtering [10].
To better understand the lower T_c in our films, we have performed Hall effect measurements and compared them to those of Suzuki [10], on films grown onto $SrTiO_3$ with different Sr content. Surprisingly, all our films present similar Hall numbers, corresponding actually to x = 0.1 (nominal Sr doping of the target, fig. 10).

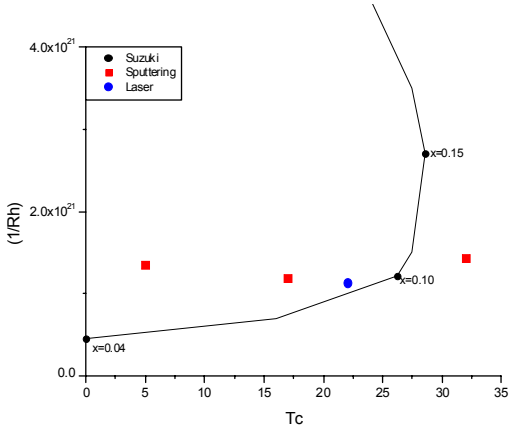

Fig. 10 : Number of carriers as a function of T_{co}.

At the same time, we made some samples with our new PLD system. This technique is supposed to preserve stochiometry better than sputtering, and we would be interested to compare the results of both methods.
Up to now, we have grown a few films and measured the Hall constant of one with T_c = 22K. Once again, we obtained a value corresponding to the nominal Sr doping (x=0.1). This seems to indicate that the Sr stochimetry is conserved in our films, so that something else should be accounted for the lower T_c, which doesn't follow the Hall number. More measurements are on course, and should be completed by a direct measurement of stochiometry by RBS (Rutherford Back-Scattering).Then we will start investigating the question of strain with series of films with different thicknesses.

Selected references

[1] M. Kugler, G. Levy de Castro, E. Giannini, A. Piriou, A. A. Manuel, C. Hess and Ø. Fischer, *J. Phys. Chem. Solids,* to be published.
[2] G. Levy de Castro, M. Kugler, A. A. Manuel, and Ø. Fischer, *J. Phys. Chem. Solids*, to be published.
[3] E. Dagotto et al, *Physics Reports* **344** (2001) 1.
[4] N. Mathur and P. Littlewood, *Phys. Today* Jan (2003) 25, M. Fäth et al, *Science* **285** (1999) 1540.
[5] P. Muralt and D. W. Pohl, Appl. *Phys. Lett.* **48** (1986) 514.
[6] B. Grévin et al, *Phys. Rev.* B 62 (2000) *8596,* B. Grévin et al*, Appl. Phys. Lett.* **80** (2002) 3979.
[7]J.P. Locquet et al., Nature **394**, 453 (1998)
[8]M. Abrecht et al., *Phys. Rev. Let.* **95-5**, 7002 (2003)
[9]H. Sato et al., *Phys. Rev*. B **621**, 12447 (2000)
[10]M. Suzuki, *Phys. Rev.* B **39-4**, 2312 (1989)

Applications of superconductivity

René Flükiger

Research summary

The research in our group is centred on crystal growth, mainly of superconducting materials, and on the analysis of metallurgical and physical properties of superconductors for practical applications. The crystal growth program comprises a series of compounds, which are of importance for various scientific aspects at the DPMC. A strong effort is devoted to the Bi-2223 system: this 3-layer compound has one of the highest known T_c values (110K), but due to the lack of single crystals of sufficient size and quality, many properties were so far still waiting to be investigated. We succeeded in refining for the first time the 5-fold orthorhombic supercell of Bi-2223. A spectacular enhancement of the irreversibility field was obtained in Pb-doped Bi-2212 crystals, by combining strong Pb-doping that removes the structure modulation, with ion irradiation.

The investigation of the transport properties under an applied magnetic field is of central interest in order to optimise the performance of MgB_2 tapes for industrial applications. Fe and Stainless Steel sheathed tapes have been fabricated either by cold or hot rolling. XRD measurements on the filaments show that the cold rolled tapes have moderate texture of the grains while hot rolling arranges grains almost randomly. The filament texture seems to be the main reason for the anisotropic critical current density, its measured values being not otherwise justified by the intrinsic anisotropy of the material. Pinning properties of MgB_2 have been studied by magnetic relaxation techniques. Transport properties under strain and applied magnetic fields are being investigated in superconducting tapes and wires of various materials (mainly Nb_3Sn). The study of the 3rd harmonics of AC magnetic susceptibility made it possible to study the Peak Effect in Nb_3Sn up to very high fields (19 T) and to relate it to the transition between a disordered vortex state and a Bragg glass state.

Crystal Growth and Characterisation

Pb-free and Pb-doped $Bi_2Sr_2Ca_2Cu_3O_{10}$ crystals

Very recently, our effort in growing crystals of $Bi_2Sr_2Ca_2Cu_3O_{10}$ superconductors was rewarded by a successful production of high quality Bi-2223 single crystals, thus allowing scanning tunnelling spectroscopy (STS), optical spectroscopy, and other experiments that were not possible before. The activity on crystal growth of Pb-free and Pb-doped Bi-2223 has continued during the last year, leading to an improvement of size and quality. By carefully controlling the density and the quality of precursors and using a very low travelling velocity (~40 μm/h), pure Bi-2223 crystals, as large as 9×5×0.8 mm^3 have been grown, a size never obtained before (Fig. 1).

The Bi-2223 phase is known to be much less sensitive to oxygen doping than the other two members of the Bi-family, Bi-2212 and Bi-2201. After annealing in O_2 at 500°C, we found a smooth dependence of T_c on $p(O_2)$, ranging from T_c = 103 K at $p(O_2) < 10^{-3}$ bar to T_c = 108 K at $p(O_2)$ = 400 bar, the optimal doping T_c= 110.5 K being achieved at $p(O_2)$ = 20 bar.

Thanks to the availability of high-quality Bi-2223 and (Bi,Pb)-2223 crystals, we have been able to study their structure by single-crystal X-Ray diffraction.

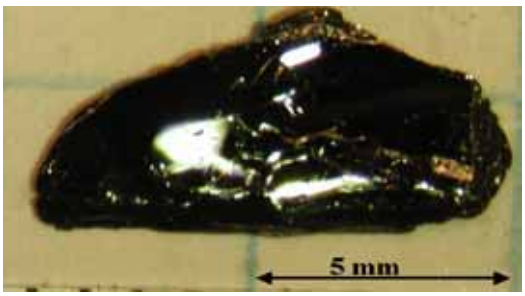

Fig. 1 : Large Bi-2223 crystal grown by the TSFZ method.

The crystal structures are characterized by an incommensurate modulation having its main component in the direction of one of the short translation vectors of the subcell, however, the structures can be conveniently described in 5-fold supercells (**q** = 0.2 **a***$_{sub}$) (Fig. 2). Additional oxygen atoms were found in the BiO layers. In both crystals an additional O atom has been inserted at the level of every 10th Bi atom, which defines the translation unit of the modulation wave. A partial substitution of Ca by Bi was also observed in both crystals. The actual compositions of the crystals are thus $Bi_{2.16}Sr_2Ca_{1.84}Cu_3O_{10.17}$ and $(Bi_{1.8}Pb_{0.2})_{2.10}Sr_2Ca_{1.90}Cu_3O_{10.19}$, respectively.

Crystal	*Bi-2223*	*Bi,Pb-2223*
Space group	*A2aa* (subcell), *P*222 (supercell)	
a_{sub} (Å)	5.4210(7)	5.3952(14)
a_{super} (Å)	27.105(4)	26.976(7)
b (Å)	5.4133(6)	5.4130(10)
c (Å)	37.010(7)	37.042(11)

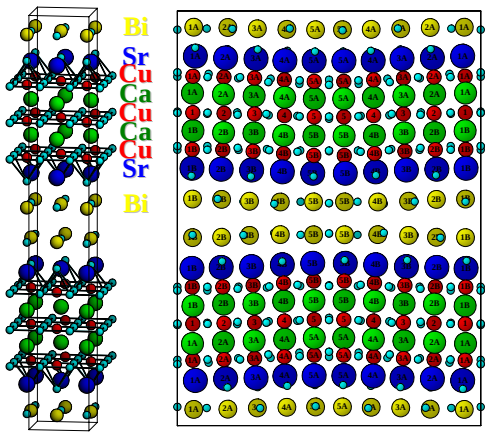

Fig.2. (left) Average structure of the Bi-2223 phase and (right) b-projection of the orthorhombic supercell. Modulated displacement along the c-axis is visible.

The structures of the $Bi_2Sr_2Ca_{n-1}Cu_nO_{4+2n+\delta}$ series have a strong two-dimensional character with weak links between the BiO layers. In the orthorhombic superstructure of Bi-2223 (n = 3), the longitudinal waves of the Bi atoms in two neighboring BiO layers are in phase and, consequently, the transverse waves are out of phase (shifted by 180°). For the monoclinic superstructures of Bi-2212 (n = 2, $\mathbf{q}$ = 0.22 $\mathbf{a}^*_{sub}$) and Bi-2201 (n = 1, $\mathbf{q}$ = 0.2 $\mathbf{a}^*_{sub}$), the phase difference between the transverse displacement waves of the Bi atoms in consecutive slabs is 160 and 72°, respectively. The amplitude of the transverse displacement wave increases with decreasing thickness of the slabs.

Crystal	*Bi-2223*	*Bi-2212*	*Bi-2201*
Slab thickness (Å)	15.378	12.224	9.109
Wavelength (Å)	27.105	24.413	26.908
Amplitude (Å)	0.139(7)	0.156(6)	0.310(7)
Phase difference	180°	160°	72°

Enhanced pinning properties in ion-irradiated modulation free Pb-doped Bi-2212 crystals.

We have successfully obtained Bi-2212 crystals with strongly enhanced pinning properties by substituting Bi atoms by Pb atoms. The large amount of Pb substituted in the structure leads to the disappearance of the structural modulation associated with the Bi-2212 phase. This structural change is the main responsible for the pinning enhancement, as it yields a large reduction of the magnetic anisotropy of the phase. In a next step, we have combined both the effects of heavy Pb doping and heavy ion irradiation of the crystals. Modulation-free heavily Pb-doped (Bi,Pb)-2212 crystals were irradiated with 5.8 GeV ions, using the facilities of GANIL (Caen). This irradiation dose is equivalent to a matching field of $H_\phi = 10^4$ Oe. In Fig. 3, we present the irreversibility lines of a pristine and an irradiated Pb-doped (Bi,Pb)-2212 crystal, as a function of the reduced temperature $t=T/T_c$. The combination of Pb-doping with ion irradiation leads to a spectacular enhancement of the irreversible portion of the H-T plane.

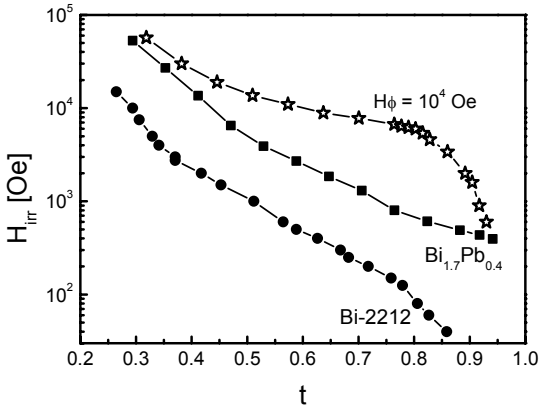

Fig. 3. $H_{irr}(T)$ lines of Pb-free Bi-2212 (●), Pb-doped Bi-2212 (■) and ion-irradiated Pb-doped Bi-2212 crystals (☆), as a function of reduced temperature $t=T/T_c$.

Vortex Phase Transition in Nb_3Sn single crystals by 3rd harmonics of the AC susceptibility

We measured the 1st and the 3rd harmonics of the AC magnetic susceptibility as a function of temperature, at DC magnetic fields up to 19 T, on a high quality single crystal of Nb_3Sn. We detected for the first time in this material the Peak Effect (PE), corresponding to a dip in the real part of the 1st harmonics, χ'_1. It is known that PE is associated to the transition of the vortex lattice between a disordered and the Bragg Glass phase. The PE disappears at $\mu_0 H > 13$ T, however, by the measurement of the 3rd harmonics, we succeeded in revealing the Bragg/disordered transition even at higher magnetic fields. The H-T phase diagram obtained by the 1st and the 3rd harmonics measurements is summarized in Fig.4, where both the Bragg Glass and the disordered phase have been displayed.

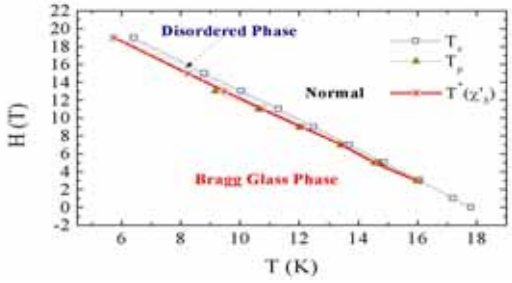

Fig. 4 : H-T Phase Diagram of Nb_3Sn single crystal.

Growth of CoSi single crystals.

Transition metal monosilicides exhibit intriguing electronic properties related to the spin-singlet formation. In collaboration with Van der Marel's group, we have grown single crystals of CoSi. A Czochraski crystal growth technique has been used, using a RF levitation furnace with a water-cooled, Hukin-type cold copper crucible. Our crystals, grown at a growth rate of 5 mm/h under overpressure of pure Ar, were characterised by XRD Laue diffraction, optical microscopy, SEM and resistivity measurements. The value of RRR=6.3, the highest obtained so far in CoSi, proves the good quality of these crystals.

Processing and characterisation of superconducting tapes and wires for practical applications

J_c anisotropy and texture in MgB_2 tapes

Fe-sheathed MgB_2 monofilamentary tapes are fabricated via the *ex-situ* powder-in-tube technique, using starting powders with various particle sizes. The fabrication steps include swaging, drawing and final rolling during which the rolls exert perpendicular and shear forces on the flat surface of the tapes. In order to study the anisotropy of the critical current density of the conductors with respect to the applied magnetic field orientation, critical current measurements vs. the applied magnetic field have been performed at 4.2 K (Fig. 5) for four tapes made of powders with sizes of 4 μm (A and B) and 1 μm (C and D).

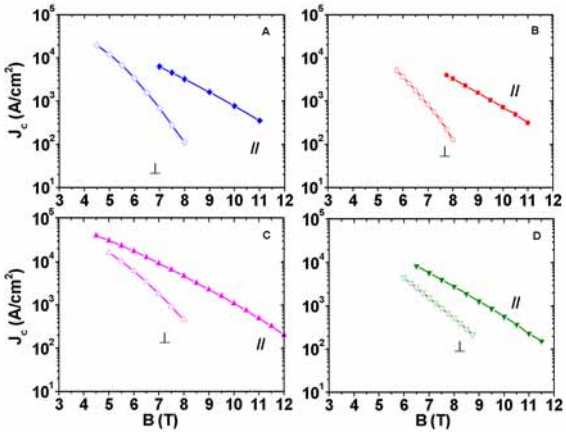

Fig. 5. Critical current density J_c for the samples A, B, C, and D at 4.2 K.

The anisotropy Γ of the critical current ($\Gamma = J_c(B_{//})/J_c(B_{\perp})$) is found to be more pronounced for the tapes prepared with the larger particle sizes (see Fig. 6). XRD measurements have been performed on the filaments extracted from the Fe sheath in order to investigate the origin of the critical current anisotropy. Due to the large penetration depth of the CuK_α radiation into the filaments (thickness 200 μm), it has been necessary to proceed to a series of measurements starting from the central part of the filament (after grinding) and successively *removing each time 25 μm of it*. The degree of preferred orientation along the *[00l]* crystallographic direction is expressed by the HWHM of the rocking curve ϕ. Fig. 7 shows the HWHM-ϕ as a function of the distance from the interface between the Fe sheath and MgB_2 filament. Near the interface with the sheath, the degree of orientation results to be more pronouced. It is thus more probable for the current to flow within the more textured layers, passing through the external part of the samples, than to flow within the internal ones. It could be possible to enhance the critical current density in ex-situ tapes by enlarging the regions with a high degree of texturing.

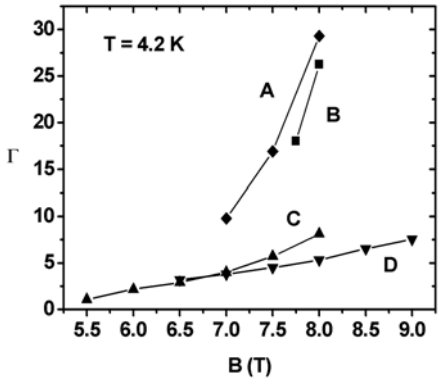

Fig. 6. Anisotropy at 4.2 K of J_c versus applied magnetic field for the tapes A, B, C, and D.

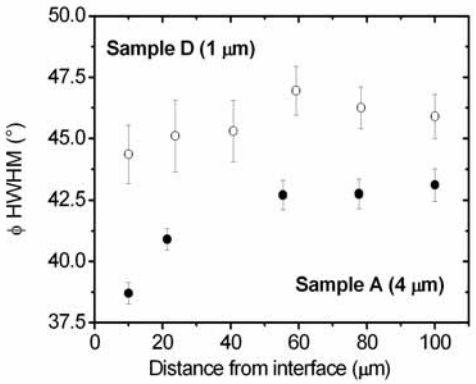

Fig. 7. FWHM of the rocking curve as a function of thickness of the filament from the interface with the Fe sheath.

Magnetic Relaxation and Pinning Properties of "ex-situ" MgB_2/Fe Tapes

The time decay of the non-equilibrium magnetization has been analysed on *ex-situ* MgB_2/Fe tapes in parallel and perpendicular magnetic field in order to investigate the correlation between the anisotropy of the pinning properties and the texturing. Magnetic relaxation

measurements have been performed in dc magnetic fields up to 9 T at temperatures varying from 5 to 35 K. The magnetization has been found to decrease linearly with ln(t). This allows to calculate the pinning potential energy U_0 by using the relationship $U_0 = kT/\{dM/[M_0 d\ln(t)]\}$. The resulting behaviour of U_0 in field and temperature is not related to the field orientation, as shown in Fig. 8. The anisotropy of the pinning energy U_0 at fixed B and T can be ascribed to the partial texturing of the tapes and, thus, to the anisotropy of the superconducting properties of MgB_2.

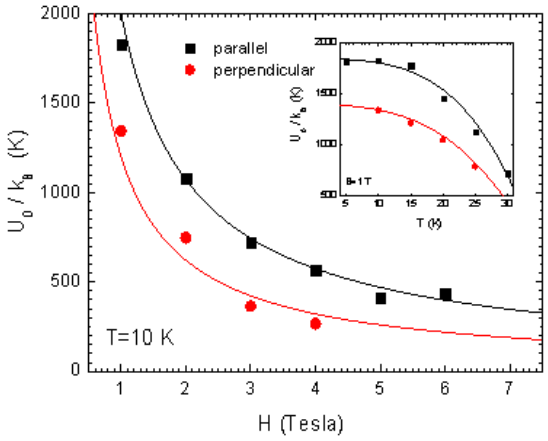

Fig. 8. Field behaviour of the pinning energy U_0 at T = 10 K extracted from the relaxation rate in parallel (black squares) and perpendicular (red circles) field; in the inset, the temperature dependence of U_0 at B_{dc} = 1 T is reported for both the field orientations.

I_C versus strain measurements in Nb_3Sn superconducting wires and tapes

In collaboration with B. Seeber and D. Uglietti (GAP-Supra) the critical current has been measured as a function of uniaxial tensile strain at 17T, 19T and 21T on two Nb_3Sn wires prepared by the "Bronze" - (GAP-Geneva) and the "Internal Sn" - Technique (Oxford Superconducting Technologies). The wire are respectively $(Nb,Ti,Ta)_3Sn$ and $(Nb,Ti)_3Sn$. In Fig.9 the $I_c(\varepsilon)$ curves at 17T and 19T are shown. The $I_c(B,\varepsilon)$ curves of the two wires have been fitted with the ten Haken and Ekin models, using the formulas below.

$$J_c(B,\varepsilon) \propto \left(\frac{B_{c2}(\varepsilon)}{B}\right)^{1-p} \cdot \left(1-\frac{B}{B_{c2}(\varepsilon)}\right)^{q}$$

where p=0.5 and q=2 and

$$B_{c2}(\varepsilon) = B_{c2}(0)\cdot\left(1-a|\varepsilon-\delta|^{1.7}\right)$$

in the Ekin's model, and

$$B_{c2}(\varepsilon) = B_{c2}(0)\cdot\frac{1-C_a\sqrt{(\varepsilon+\delta)^2+\varepsilon_0^2}}{1-C_a\varepsilon_0}$$

in the ten Haken model.

In the Ekin model, the fit parameters are B_{c2}, a and δ, whereas the ten Haken model has one parameter more: B_{c2}, C_a, ε_0 and δ. The parameter δ is the so-called thermal induced pre-strain ($\delta \sim 0.25\%$ for both wires). According to the authors, the parameters C_a, ε_0 and a, should be material constants, so they should have the same value in both wires ("Bronze" and "Internal Sn"). That means that the only parameter that has an influence on the shape of the $I_c(B,\varepsilon)$ curve is B_{c2}. From the I_c *vs.* B curves, it appears that the critical field is about the same in both wires, so the $I_c(\varepsilon)$ curve is expected to have the same slope in both wires. It is not the case: the curve is much steeper for the Internal Sn wire than for the Bronze one. Both analytical and FEM calculations are in progress to determine the effect of the radial pre-strain on the critical current, taking into account the different wire design, i.e. thick, hollow filaments (Internal Sn wire) *vs.* thin solid filaments (Bronze wire). Further measurements on $(Nb,Ta)_3Sn$ and $(Nb,Ti,Ta)_3Sn$ Internal Sn wires will explore the effect of the doping on the strain and field behaviour of the critical current.

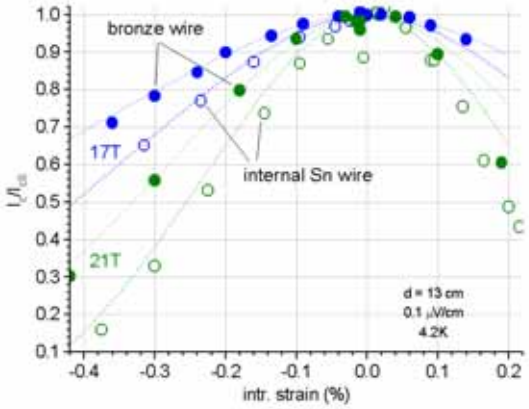

Fig. 9. Reduced critical current versus strain at 17T and 21T for the Bronze and Internal Sn wires.

Selected references

E.Giannini, V.Garnier, R. Gladyshevskii, and R. Flükiger, *Supercond. Sci. Technol.* 17 (2004) 220.

N.Clayton, N.Musolino, E.Giannini, and R. Flükiger, *Supercond. Sci. Technol.* 17 (2004) S563.

R. Gladyshevskii, N. Musolino, and R.Flükiger, *Phys. Rev. B* 70 (2004) 184522.

N. Musolino, N.Clayton, and R.Flükiger, *Phys. C* 417 (2004) 40.

P.Lezza, V.Abächerli, N.Clayton, C.Senatore, D.Uglietti, H.L.Suo, and R.Flükiger, *Phys. C* **401** (2004) 305.

Theory of condensed matter

Thierry Giamarchi

Research summary: The group works on the theory of condensed matter, in connection with various experimental groups. The research activities include the study of strongly correlated electronic systems, ab initio calculations, disordered elastic systems and quantum magnetism. For strongly correlated systems the main focus has been to understand out of equilibrium phenomena, such as tunnelling and transport, and to study the dimensional crossover in quasi-one dimensional structures, such as organic superconductors and ultra-cold atoms in optical lattices. For disordered elastic systems, the physical properties such as specific heat, diffraction spectrum and transport of periodic systems have been analysed, as well as the slow motion (creep) of domain walls. Ab initio calculations have been used to study magnetic properties of systems such as FeSi, and to study the spin-phonon coupling in High Tc systems. Density of states of two dimensional artifical solids has been studied. For quantum spin systems, the effect of spin phonon coupling and impurities has been looked at for one dimensional systems, while variational calculations have been used to determine the properties of spins and charges on a two dimensional triangular lattice.

Quasi-one dimensional systems

We examined the physical properties of quasi-one dimensional systems. Such an analysis is relevant both for organic superconductors and for cold atoms in optical lattices where such fermionic systems can now be realized.

In cold atoms systems, an unprecedented level of control can be reached, so the hopping parameters for the two spins (isospins in that case) species can be independently controlled. In collaboration with M.A. Cazalilla and A.F. Ho, we thus examined the properties of a one dimensional Hubbard model with spin-dependent hoppings. Such a system has a much richer phase diagram than the standard Hubbard model. In particular the system becomes massive in the spin sector as soon as the two velocities for spin up and down particles are different (see Fig. 1).

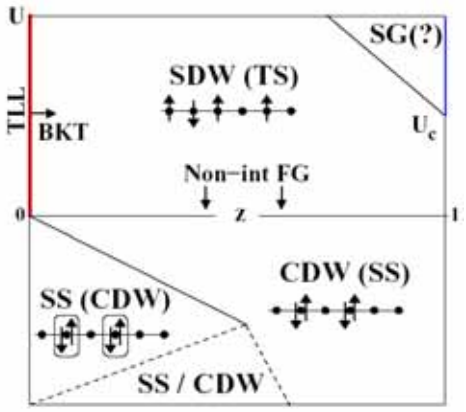

Fig.1. Phase diagram of a one dimensional Hubbard model with two different velocities for spin up and down particles. z is the velocity difference and U the interaction. Contrarily to the standard Hubbard model which has a Tomonaga-Luttinger-Liquid phase (TLL) such a system develops a spin gap. The various instabilities are a spin (or charge) density wave SDW (CDW), or singlet (triplet) superconductivity SS (TS). At too large velocitiy difference phase segregation can exist (SG).

For an isolated tube, the system is dominated by anisotropic antiferromagnetic fluctuations. When the coupling between the tubes is included, the system can stabilize a triplet superconducting phase. The existence of this phase, and the presence of a gap in the spin sector, can be detected by measuring the spin flip susceptibility by Raman laser [1].

Another system where this question of coupled tubes is relevant, is provided by the organic salts $(TMTSF)_2X$ and $(TMTTF)_2X$ that are extremely anisotropic conductors with a quarter-filled conduction band. These materials are believed to undergo a deconfinement transition as the temperature is lowered, crossing over from a 1D Luttinger-liquid phase to a 2D Fermi-liquid like phase [2]. The precise nature of the low-temperature phase is still largely unknown: in particular, many questions remain about its spectral properties, such as the possible existence of "hot spots" on the Fermi surface. As a first step towards the solution of this question we have considered a model of spinless fermions at half-filling. This system has the same density as the quarter-filled Hubbard chain, but does not break particle-hole symmetry. For solving this model we have developed a new code within the Quantum Monte Carlo – Dynamical Mean Field framework. With this code we were able to compute the Luttinger exponent K of the isolated chain—which characterizes the decay of the correlation functions—as a function of the in-chain interaction strength. The numerical results are consistent with the known analytical results. The extension of this analysis to the case of coupled chains and to the study of the deconfinement transition are in progress.

Another important question for the organics is the nature of the superconducting phase. It was observed during recent years that, at low temperatures, certain superconducting organic

compounds show upper critical fields in excess of the Pauli-Clogston paramagnetic limit; usually depending on the angular orientation of the field with respect to the crystalline axes. High critical fields constitute an indication of possible triplet-pairing superconducting phases. An unambiguous interpretation of this effect is of course difficult and independent confirmations of the unconventional paring scenario are therefore desirable. A large number of independent experimental checks were both proposed and some carried out. We were concerned with the relevant signatures of triplet superconductivity to be found in proposed point-contact tunneling experiments.

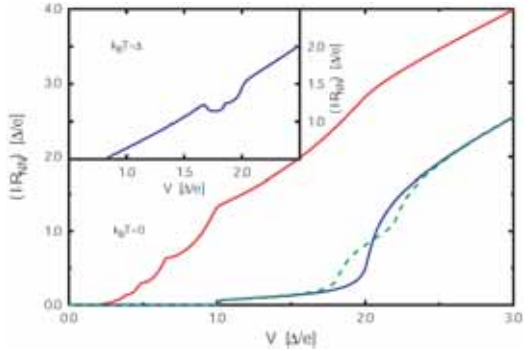

Fig.2. Different sets of I-V characteristics for point contact junctions. Red curve is an S-S junction. The structure below the gap is due to the Andreev reflections. The blue and green curves are for an S-T junction, with and without magnetic field respectively. In the insert is a finite temperature curve for a S-S with two different gaps.

We developped a microscopic calculation of tunneling in superconducting junctions based on a non-equilibrium Green function formalism to incorporate the case of spin-triplet pairing. We have studied the efect of finite temperatures and magnetic fields, and have shown that distinctive features are present in the I-V characteristics of different kinds of junctions; in particular when the Zeeman effect of a magnetic field is taken into account (see Fig. 2). The observation of such features would constitute a sensitive experiment that permits to identify the type of pairing [3].

Disordered elastic systems

Understanding the physical properties of disordered elastic systems is a challenging question relevant to a host of experimental situations ranging from periodic ones, such as vortex lattices, charge density waves, Wigner crystals, to interfaces, such as magnetic or ferroelectric domain walls, fluid invasion in porous media, contact lines of liquid menisci on a rough substrate and domain growth. A paradigmatic but still poorly understood problem is the creep motion of an elastic string in a two dimensional pinning landscape. We have addressed this problem by means of Langevin dynamics simulations. We find that the Velocity-Force characteristics are well described by the creep formula predicted from phenomenological scaling arguments. We have analyzed the creep exponent μ, and the roughness exponent ζ. Two regimes are identified: when the temperature is larger than the strength of the disorder we find $\mu \cong 1/4$ and $\zeta \cong 2/3$, in agreement with the quasi-equilibrium-nucleation picture of creep motion; on the contrary, lowering enough the temperature, the values of μ and ζ increase showing a strong violation of the latter picture (see Fig. 3) [4].

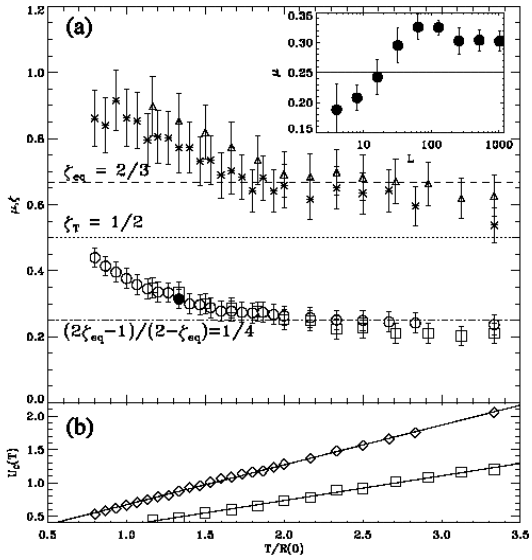

Fig.3. (a) Roughness exponent ζ and creep exponent μ as a function of temperature T. Deviations from the phenomenological predictions ζ=2/3, μ=1/4 are clearly seen at low temperatures. (b) Temperature dependence of the characteristic energy barrier Uc.

We have also put in evidence the underlying connection between the critical properties of the depinning transition and the extreme value statistics of correlated variables. We found the distribution to be Gaussian for all periodic systems, while in the case of random manifolds there exists a family of universal functions ranging from the Gaussian to the Gumbel distribution (see Fig. 4) [5].

For the case of periodic systems, it was recently shown, that the positional order of these systems is only algebraically destroyed leading to divergent Bragg peaks and a nearly perfect crystal state.

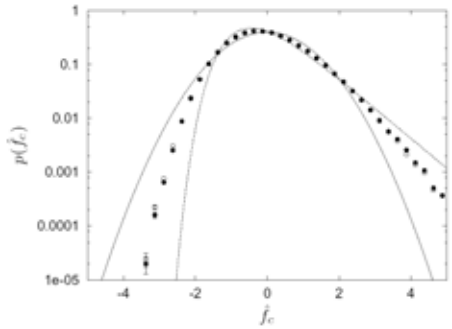

Fig.4 Example of a numerically determined curve belonging to the newly found universal family of functions that interpolates between the Gaussian distribution (solid line) and the Gumbel one (dashed line) in the case of random manifold systems.

Quite remarkably, it was shown that for weak disorder this solution is stable to the proliferation of topological defects, and thus that a thermodynamically stable phase having both glassy properties and quasi-long range positional order exists. This phase, nicknamed Bragg glass, has prompted many further analytical and experimental studies. Although its existence can be tested indirectly by the consequences on the phase diagram of vortex flux lines, the most direct proof is to measure the predicted algebraic decay of the positional order. Such a measurement can be done by means of diffraction experiments, using either neutrons or X-rays on the crystal. Neutron diffraction experiments have recently provided unambiguous evidence of the existence of the Bragg glass phase for vortex lattices.

Another periodic system in which one can expect a Bragg glass to occur are CDWs, where the electronic density shows a sinusoidal modulation. As a consequence of the elecron-phonon interaction, this modulation generates a permanent distortion of the underlying lattice. This distorsion can be revealed thanks to X-ray spectrum : the corresponding X-ray spectrum presents satellite peaks around each principal Bragg peak. These satellites contain information concerning the positional order of the CDW. The X–ray experimental resolution is in principle much higher than the one that can be achieved by neutrons for vortex lattices, consequently CDW systems should be prime candidates to check for the existence of a Bragg glass state. However, compared to the case of vortex lattices the interpretation of the spectrum is much more complicated for two main reasons: (i) the phase of the CDW is the object described by an elastic energy, whereas the X-ray probes the displacements of the atoms in the crystal lattice (essentially a cosine of the phase); (ii) since the impurities substitute some atoms of the crystal, the very presence of the impurities changes the X-ray spectrum. This generates non-trivial terms of interference between disorder and atomic displacements. It is thus necessary to make a detailed theoretical analysis for the diffraction due to a pinned CDW. In the past the study of the spectrum has been carried out only either for strong pinning or at high temperatures. We have focused our attention on the low temperature limit where a well formed CDW exists and on weak disorder, for which one expects to be in the Bragg glass regime. Both the short and long range screening of the Coulomb interactions were considered. We have shown that in both cases the diffraction spectrum consists in two asymmetric peaks (see Fig. 5).

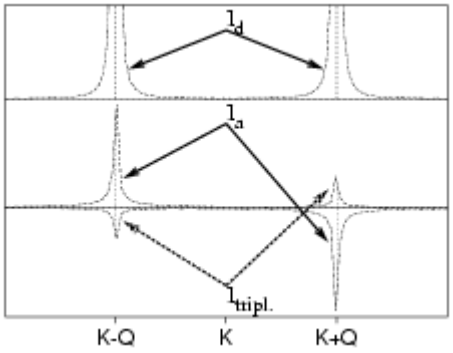

Fig.5. Intensities of the different contributions to satellite peaks. The more divergent term, I_d , is symmetric. I_a and $I_{tripl.}$ are antisymmetric.

The peaks are power-law divergent, with a stronger anisotropic shape in the case of unscreened long-range Coulomb interaction. This finding is consistent with the Bragg glass behavior. The asymmetry divergence follows a subdominant power-law as well, with an exponent that we have also determined [6].

With G. Schehr and P. le Doussal, we have examined the specific heat of such periodic disordered glassy systems. We have shown that contrarily to the standard expected result of specific heat linear in temperature (as predicted e.g. by the phenomenological model of two level systems), disordered elastic systems have a specific heat varying as T^3 at low temperatures (for all dimensions below d=4). The coefficient is determined by the pinning (Larkin) length. This cancellation of the linear term seems quite general and occurs also in other types of quantum glassy systems [7].

For quantum systems, a similar competition exists, leading to phases such as the Wigner glass or the Coulomb glass. Recent experimental studies of hopping conductance in Anderson Insulators showed striking nonequilibrium effects that persist for very long times at low temperatures. We investigated this

issue by kinetic Monte Carlo simulations. Our results (see Fig. 6) suggest a transition from stationary to nonstationary dynamics at the equilibrium glass transition temperature of the system.

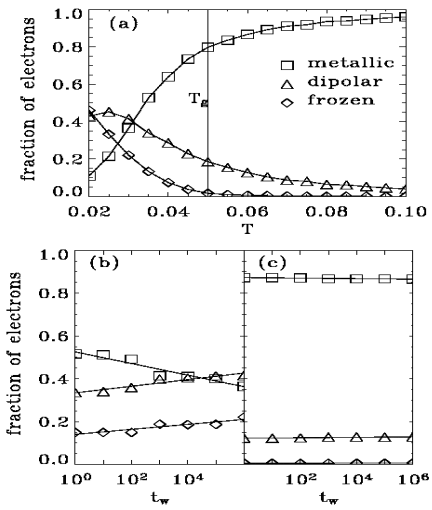

Fig.6. Temperature T (a) and waiting time tw dependence at low (b), and high temperatures (c), of the occupancy of the dynamical modes of electrons during the relaxation of the Coulomb glass.

Within a selected time interval two group of carriers are identified: electrons whose motion is diffusive and electrons that remain confined in small regions of space. During the relaxation that follows a temperature quench an exchange of electrons between these two modes takes place and the nonequilibrium excess of diffusive electrons initially present decreases with time as the system relaxes. This bimodal dynamical hetereogeneity persists at higher temperature when normal electron diffusion and stationarity is recovered. The temperature dependence of the occupancy of the two dynamical modes reflects a crossover between a low-temperature regime with a high concentration of electrons forming fluctuating dipoles and a high temperature regime in wich the concentration of diffusive electrons is high [8].

Electronic structures

Various properties involving the electronic structure of either regular or artificially built materials have been investigated.

The B20 structure is the stable structure of the much studied MnSi, FeSi, CoSi, FeGe etc., and the question has been posed whether strong correlation is important for the onset of magnetism at some compositions. Our calculations of the properties of these systems include no assumptions of strong correlation. Extensive spectroscopic measurements (see the group of D. van der Marel) on several of the B20 compounds have motivated us to do calculations of the spectroscopic properties from the LDA band structure.

Ferromagnetic MnSi is found to have a sudden transition from a low moment (~0.4 μ_B per MnSi) to a high moment state (~0.8 μ_B) when the lattice constant increases from 8.3 to 8.35 a.u.(see Fig. 7). Saturation moment at ambient pressure suggests that the moment is about 0.4, and our calculated hyperfine field on Mn (−60 kOe) is consistent with this value.

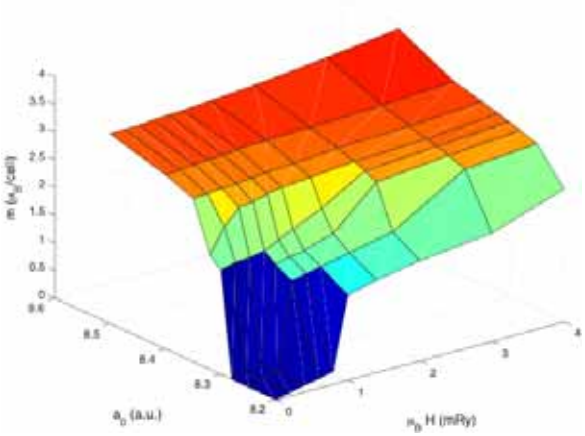

Fig.7. Magnetic moment per cell (4 MnSi) as function of lattice constant and applied magnetic field.

Indications of a high moment solution (much larger than 1 μ_B) from Mn-2*p* and Mn-3*s* XAS spectra suggested calculations of these spectra as function of the moment through variations of the lattice constant. These calculations are made for supercells in which one atom has a core hole. However, the band results cannot find the very large moments as the Hund rule gives for free Mn, and the calculated XAS spectra are different from the observations of the high spin state in MnO. The complementary SXE spectrum, probing the occupied DOS, is consistent with the low spin solution, although the resolution prevents a precise comparison with experiment. The calculated XAS agree well with experiment for non magnetic CoSi, while for FM MnSi and paramagnetic FeSi the comparison is less good.

The unusual properties of FeSi have previously been explained as an effect of thermal disorder. Later measurements showed that the degree of disorder used in the calculations is of the correct order. However, the issue of non-conservation of spectral weight, seen in optical measurements, was not considered in our calculations. Preliminary results show that structural and magnetic disorder at larger *T* can modify the spectral weight, but also that variation of the ordered magnetic moment plays a role. A

substantial exchange enhancement will follow when the narrow gap is filled by thermal fluctuations, and this will increase the spectral weight at low excitation energies. The different corrections to the spectral weight from the one particle results can be opposite, and the details of the band structure will determine if there is an increase or decrease with *T*.
FeGe is similar to FeSi, but the gap is closed at ambient pressure with a FM ground state. The calculations as function of pressure show that the gap should reappear at about 0.1 Mbar. The exchange enhancement will peak for intermediate pressures, with possibilities for superconductivity mediated by spin fluctuations, although the lattice symmetry is expected to prevent a large T_c [9].

In MnSi calculations of the positron distribution have been performed. The positron probes mostly the Mn sites and ACAR measurements should give information of the Fermi surface topology. The topology of the Fermi surfaces of the two spins will change with the size of the moment. Positron annihilation will therefore give an indirect and sensitive probe of the FM state, and this and investigations on other alloys are made in collaboration with the group in Bristol.

Calculations of phonon and spin waves of large wave lengths have been performed for La and Hg based high-T_c oxides. The results indicate that the coupling is larger for larger wave length, corresponding to less doping. But the amplitude of λ_{sf}, is too low when using LDSA, and a bit lower for the La than in the Hg-based case. By doing calculations with non-optimal choice of linearization energies, it is possible to obtain near AFM order for the undoped La based copper oxide (as shown previously for the Hg based case), and enhanced λ_{sf} for the doped cases, and this is still within LDSA. Corrections of LDSA have been attempted, where exchange and correlation potential depends on kinetic energy and non-locality. This leads to stronger antiferromagnetic fluctuations, as in the calculations with modified linearization, but the convergence is not sufficient for quantitative results of λ_{sf}.

We have analyzed by tight-binding theoretical modelling (in collaboration with F. Mila) the local density of state of a two-dimensional superlattice of Ce adatoms on a Ag(111) surface that has been determined by Scanning Tunneling Spectroscopy at 3.9 K (by the group of W.-D. Schneider). We have explored the local electronic structure of a unique adatom superlattice, a 2D hexagonal superlattice of Ce adatoms on a Ag(111) surface.

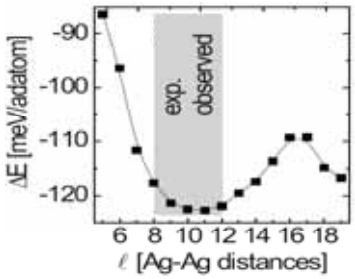

Fig.8. Difference of the electronic energy between the silver surface with a Cerium covering of unit-cell size l^2 and the clean surface. The electronic energy is normalized by the number of Cerium atoms. We find that the most favorable configuration corresponds to a Ce-Ce distance of 3.2 nm, precisely the distance realized experimentally in most cases.

The distance between two Ce adatoms in this superlattice depends on the Ce coverage, and was determined experimentally with scanning tunneling microscopy to be in the range of d = 2.3 to 3.5 nm. For a given superlattice spacing d, the formation of a new 2D mini-Brillouin zone with a concomitant splitting of the Ag(111) surface state band is expected. We observed characteristic spectral structures and spectroscopic images which were successfully modelled within a TB description of the 2D bandstructure, showing the opening of gaps at highsymmetry points of the superlattice Brillouin zone. In particular, the model accurately predicts the range of superlattice adatom spacings d observed for stable superlattices, as well as the influence of the adatom spacing d and local disorder on the local electronic structure. The scattering of Ag(111) surface state electrons by the Ce adatom superlattice leads to gap openings and to LDOS singularities at highsymmetry points of the surface mini-Brillouin zone which agree quantitatively with the characteristic features observed in differential conductance (dI/dV) spectra. In addition, the energy gain associated with the gap formation is maximal for superlattices with adatom distances in the range *2.3−3.5* nm, in excellent agreement with experiments (see Fig. 8) [10].

Low dimensional spin systems

We investigated various aspects of low dimensional magnetism. Indeed in low dimension or on special lattices quantum fluctuations and/or frustration lead to quite unusual spin properties.

We examined, in collaboration with R. Citro and E. Orignac, the properties of one dimensional spin chains in presence of lattice phonons. It is well known in that case that, for classical lattice distortions, the one dimensional spin chain is unstable to lattice dimerization leading to the so

called spin-Peierls distortion and the formation of spin singlets. For the case of quantum phonons the situation is more complicated and people have usually resorted to either treating the phonons classically (so called adiabatic limit) or assuming that the phonons are so fast that they can be integrated out and simply lead to additional spin-spin couplings (anti-adiabatic limit). However many experimental compounds are clearly between these two extreme cases. We developed both a variational and a renormalization procedure allowing to treat the full crossover between this two cases and to compute the physical properties of a generic spin-Peierls system. This approach allows to unify and interpret all previous numerical analysis on such spin-Peierls systems (see Fig. 9), as well as to give a consistent description of experimental compounds [11].

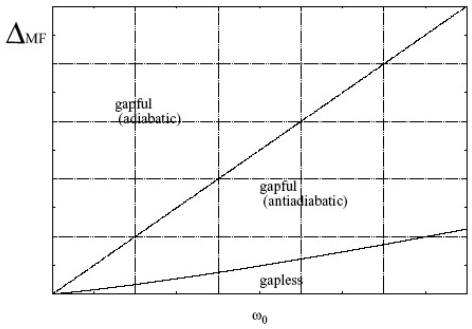

Fig.9. Phase diagram for a spin Peierls system. ω_0 is the characteristic phonon frequency of the lattice distortions. Δ_{MF} is the mean-field spin-Peierls gap which is proprotional to the electron-phonon coupling.

With L. Benfatto, we looked at the effect of spin ½ impurities in a spin chain. Such a problem is known to be a realization of a two channel Kondo problem. Using a bosonization representation we can describe the single impurity correlations. This should allow to successfully tackling the case of a large number of impurities. This study is currently ongoing.

The recent discovery of superconductivity at low temperatures in the triangular CoO_2 ($Na_xCoO_2.yH_2O$) layered compounds is an interesting event, since it may be the long sought low-temperature resonating valence bond superconductor, on a lattice which was at the basis of Anderson's original ideas on a possible quantum spin liquid state. It was pointed out that this system may be viewed as a spin-1/2 Mott insulator with electron doping of x=35%. Thus, this compound can be well described by the t-J model on a triangular lattice. RVB mean-field theory and slave-boson mean-field theory were used in the *t-J* model on a triangular lattice with finite doping : a superconducting ground state with a $d_{x2-y2} + id_{xy}$ pairing was found over significant range of doping. However, the mean-field theories involve approximations, and it is sometimes difficult to sort the artefacts due to the approximations from the true features of the model. We thus studied the different kinds of instabilites in the *t-J* model on a triangular lattice within the framework of variational Monte Carlo (VMC). The VMC method provides variational upper bounds for the ground-state energy, which can be considered exact up to the eventually residual bias due to finite-size effects. We have proposed a variational wave-function mixing the following instabilities : the 120° magnetic phase, the $d_{x2-y2} + id_{xy}$ RVB phase and finally a staggered flux phase. It was found that the resulting wave-function could be extended in terms of a sum of Pfaffians.

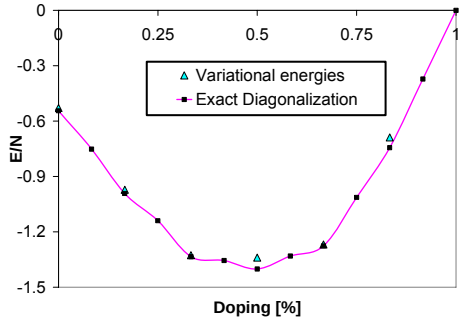

Fig.10. Energy per site of the t-J model versus doping for a 12-sites cluster. The variational energies (triangles) are compared with the exact energies (squares). The line is a guide for the eye.

As a first step, we have compared the variational energies with the energies we got from exact diagonalization measured on a small cluster (12-sites, see Fig.10.). We found a good agreement. Moreover we found very surprisingly that the 120° magnetization order parameter is vanishing at high doping of the order of 35%.

For more details, references and further readings see:

[1] A.F. Ho, M. A. Cazalilla and T. Giamarchi, Phys. Rev. Lett. **92**, 130405 (2004); *ibid.* cond-mat/0502487.
[2] T. Giamarchi, Chem. Rev. **104** 5037 (2004).
[3] C. J. Bolech and T. Giamarchi, Phys. Rev. Lett. **92**, 127001 (2004); *ibid.* Phys. Rev. B **71**, 024517 (2005)
[4] A. B. Kolton, A. Rosso and T.Giamarchi., Phys. Rev. Lett. **94**, 047002 (2004).
[5] C. J. Bolech and A. Rosso, Phys. Rev. Lett. **93**, 125701 (2004).
[6] A. Rosso and Giamarchi, Phys. Rev. B 70, 224204 (2004).
[7] G. Schehr, T. Giamarchi and P. le Doussal Europhys. Lett. **66**, 538 (2004); *ibid.* cond-mat/0411227.
[8] A. B. Kolton, D. Grempel and D.Dominguez, Phys. Rev. B **71***, 024206 (2005).*
[9] T. Jarlborg, J. of Magn. and Magn. Mat. **283** 238 (2004)
[10] M.Ternes, C. Weber, M. Pivetta, F. Patthey, J. P. Pelz, T. Giamarchi, F. Mila and W.-D. Schneider, Phys. Rev. Lett. **93**, 146805 (2004).
[11] R. Citro, E. Orignac and T. Giamarchi, cond-mat/0411256.

Thermodynamic data for superconductors at high field and high pressure

Alain Junod

Research summary: our group specialises in thermodynamic studies of superconductors and new materials. After having characterized MgB_2 as a two-gap superconductor by bulk methods, we turned to another superconducting boride, ZrB_{12}. Specific heat, magnetization, resistivity, and thermal expansion measurements on single crystals revealed unusual features such as type-II/1 superconductivity and electron-phonon coupling essentially given by a single anharmonic low-frequency mode. Information on the phonon and electron-phonon scattering spectra was obtained by inversion of the specific heat and resistivity curves. Research was continued in high-temperature superconductivity. First results were obtained with the specific heat of $YBa_2Cu_3O_7$ under pressure up to 10 GPa. The issue of d-wave superconductivity in detwinned $YBa_2Cu_3O_7$ was addressed using a bulk test, with surprisingly negative results. Midway between high- and low-temperature superconductivity, we studied the mixed-state specific heat of $PbMo_6S_8$, a Chevrel phase characterized by a very small value of the coherence length, searching for the effect of quantization of orbits in the vortex cores. New experimental techniques in small-sample calorimetry were developed.

$PbMo_6S_8$, midway between LTS and HTS

Most interesting effects in the phenomenogy of high-temperature superconductors (HTS) arise from the small and anisotropic value of the coherence length ξ. With $\xi \cong 2.5$ nm, the nearly isotropic Chevrel-phase superconductor $PbMo_6S_8$ only lies a factor of ~2 away from typical HTS. Specific heat experiments on new samples (collaboration with B. Seeber and R. Flükiger, Geneva) were performed to identify fluctuation effects at the superconducting transition, and to detect the signature of quantization of orbits in vortex cores (Fig. 1). Indeed the broadening of the transition in high fields can be described in the framework of finite-size effects where the divergence of the correlation length $\xi \sim |T-T_c|^{-0.67}$ is limited by inter-vortex distance $a \sim H^{-1/2}$, thus giving rise to the scaling property shown in the inset of Fig. 1. In low fields, scaling no longer holds exactly because of the limitations due to sample inhomoneneity.

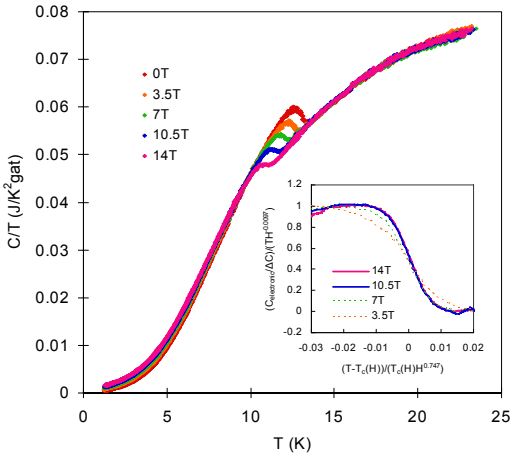

Fig.1. Specific heat of $PbMo_6S_8$ in fields of 0-14 T. Inset: scaling plot of the specific heat near T_c

At low temperature (i.e. typically $T < T_c/2$), the difference between the specific heat C/T in a field and that in zero field (Fig. 2) should be given by $\gamma H/H_{c2}$ in the continuum limit of the model of Caroli, Matricon and de Gennes (γ is the Sommerfeld constant). In the opposite limit, minigaps associated with the quantization of levels in the vortex cores should give rise to an activated behavior. We find an intermediate shape rather following a power law $C/T = a(H)+b(H)T^2$. Theoretical understanding is under way in collaboration with K. Machida (Okayama).

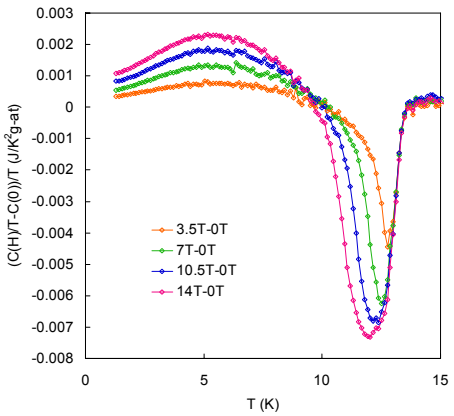

Fig.2. Difference between the specific heat of $PbMo_6S_8$ in a field and that in zero field. The vortex core contribution is visible on the left, the superconducting anomaly on the right.

Strongly coupled anharmonic phonons and type II/1 superconductivity in ZrB_{12}

The 6 K superconductor ZrB_{12}, for which data published in the literature tend to be conflicting, was investigated with two purposes in mind: characterize its phonon structure in relation to superconductivity, and map its phase diagram in the field-temperature coordinates. We performed specific heat (C), thermal expansion (α) and resistivity (R) measurements on a single crystal.

The linear behavior of α between 100 and 300 K (Fig. 3) is characteristic of a Debye temperature much larger than room temperature, a fact confirmed by the analysis of the specific heat. The broad anormaly around 50 K reflects the presence of a low-lying phonon mode. A fit using an Einstein oscillator (T_E^{α} = 170 K) and a Debye spectrum (θ_D^{α} = 1400 K) reveals considerable weighting of the T_E^{α} component. This evidences a large anharmonicity.

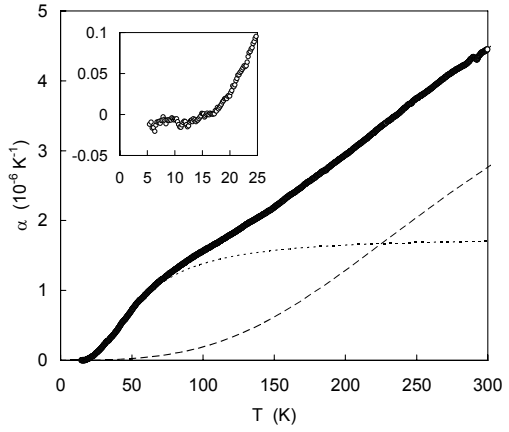

Fig.3. Linear thermal expansivity of ZrB_{12} versus temperature. The dotted and dashed lines show Einstein and Debye components, respectively. The smallness of the step at T_c = 6 K (inset) thermodynamically implies that T_c is nearly optimal with respect to the cell volume.

This low-lying phonon mode is also apparent in the shape of the specific heat and the resistivity curves, which were measured up to 300 K. By inversion procedures, we evaluated the phonon density of states $F(\omega)$ and the spectral electron-phonon scattering function $\alpha_{tr}^2F(\omega)$ (Fig. 4). The low energy mode is heavily weighted in $\alpha_{tr}^2F(\omega)$, indicating that this region provides most of the superconducting coupling.

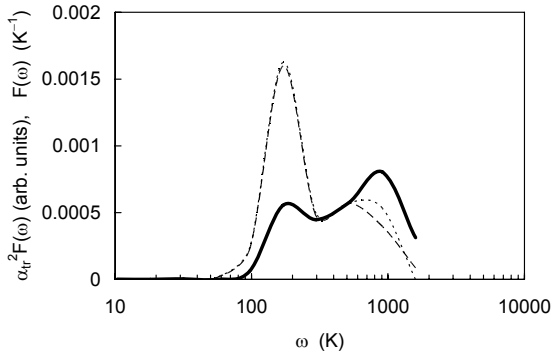

Fig.4. Full line: phonon density of states $F(\omega)$ obtained by inversion of specific heat. Dotted line and dashed line: spectral electron-phonon scattering function $\alpha_{tr}^2F(\omega)$ obtained by inversion of two resistivity measurements.

Figure 5 shows the electronic specific heat of ZrB_{12} at fixed temperature and variable field. At temperatures close to T_c, the superconducting to normal-state transition manifests itself both by a peak (i.e., a latent heat) and a step, which is characteristic of type-I superconductivity. The peaks and steps start to move apart with decreasing temperature. This indicates a crossover to type-II behavior at ~4.7 K, where the critical fields $H_{c1}(T)$ and $H_{c2}(T)$ separate from the thermodynamic critical field $H_c(T)$. This is a consequence of the Maki parameter $\kappa_1(T) = H_{c2}/\sqrt{2}H_c$ being slightly below the critical value of $2^{-1/2}$, and of its temperature dependence. The persistence of the peak at $H_{c1}(T)$, and more spectacularly of a discontinuity in the magnetization at $H_{c1}(T)$, show that the sample is in fact a type II/1 superconductor. This special behavior is associated with an attractive component in the vortex-vortex interaction.

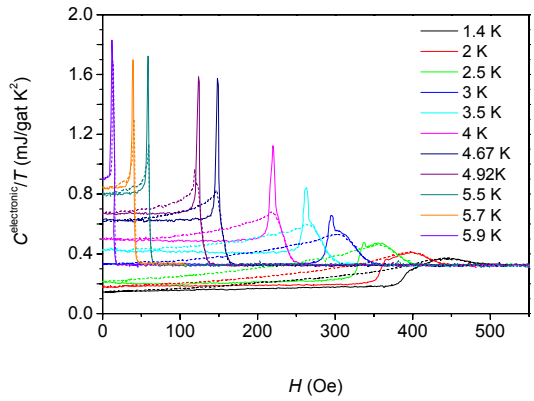

Fig.5. AC specific heat of a single crystal of ZrB_{12} in field sweeps at fixed temperatures, dB/dt > 0 in zero-field cooled conditions (full lines) followed by dB/dt < 0 (dotted lines).

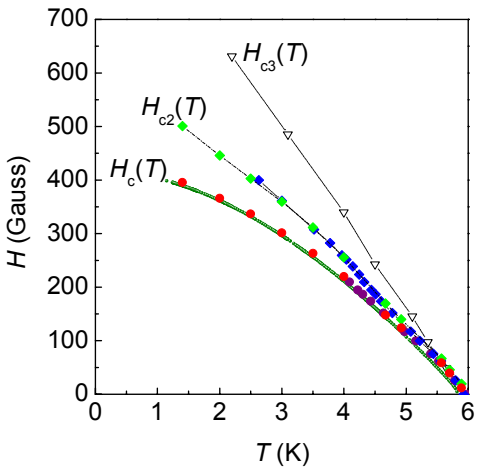

Fig.6. Phase diagram of ZrB_{12} obtained by specific-heat, magnetization, and resistivity measurements. The H_{c3} line marks the point where R = 0. At H_{c2} diamagnetism begins. The H_c curve is calculated from the specific heat difference $C_s(H=0,T)-C_n(T)$ (green line). Circles close to the H_c line mark the position of specific heat peaks and magnetization jumps. Below $H_{c1} \cong H_c$ the sample is in the Meissner state.

The resistance of ZrB_{12} does not vanish at H_{c2}(T), but at a distinct surface critical field H_{c3}(T). This rarely observed phenomenon only gives rise to a vanishingly small anomaly in the magnetization loops. All critical fields are shown in the phase diagram of Fig. 6. (Collaboration with Yu. Paderno, Kiev, and V. Gasparov, Chernogolovka).

Specific heat of Y-123 at high pressure

Till now, AC specific-heat measurements under high pressure up to several GPa in Bridgman-type pressure cells have been limited to samples with a large heat capacity at low temperatures, e.g. heavy-fermions, while it is widely believed that it might become increasingly difficult at higher temperatures. We developed this method further to study the tiny (~1%) specific-heat anomaly at the transition temperature T_c of high-temperature superconductors under the influence of pressure up to 10 GPa.

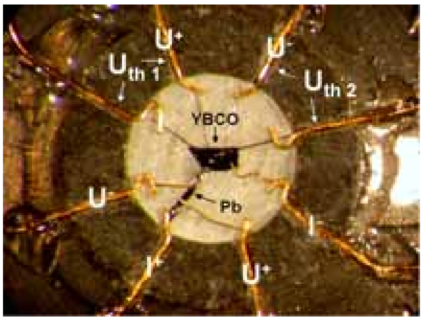

Fig.7. Assembly of sample, thermocouples and current leads on a disc of steatite (white) inside a gasket (grey) mounted on one of the anvils of a pressure cell to perform specific-heat and resistivity measurements. The steatite disc serves as a pressure-transmitting medium. A second disc of steatite (not shown) is laid on top of this assembly before closing the cell. The total thickness of the pressure cell is 250 μm.

Measurements have been performed on a stoichometric, overdoped, and detwinned $YBa_2Cu_3O_7$ single crystal, in order to investigate the pressure dependence of T_c, the shape of the specific-heat anomaly, and the superconducting condensation energy in the overdoped range of the phase diagram. The value of T_c, as obtained from specific-heat measurements, represents the real bulk T_c which might differ from that obtained by standard high-pressure techniques such as AC susceptibility or resistivity. T_c decreases by about 10 K under the application of 10 GPa, whereas only minor changes in the size of the anomaly ΔC (which is closely related to the superconducting condensation energy) are found. This behavior contrasts with that known on the underdoped side of the phase diagram of HTS: for a comparable T_c change, ΔC has been reported to decrease by a factor of ~4 [1]. The shape of the specific-heat anomaly is not drastically modified versus pressure, reflecting the absence of strong phase fluctuations or the absence of a pseudogap above T_c in the overdoped range.[2]
The results are in agreement with a simple charge-transfer model where the leading effect of pressure is doping. Applying high pressure to high-temperature superconductors thus represents a clean method to change the charge-carrier concentration of stoichometric samples without adding disorder. It confirms results obtained on Ca-doped samples.[1] (Collaboration with D. Jaccard, Geneva, and S. Tajima, Tokyo)

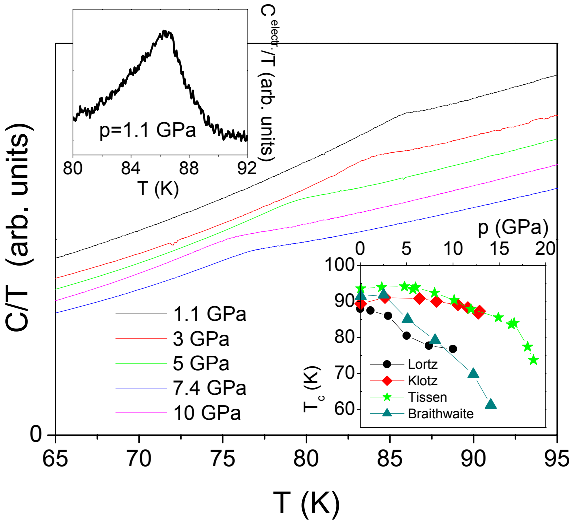

Fig.8. Specific heat C/T of a single crystal of $YBa_2Cu_3O_7$ (including some contribution from the pressure transmitting medium, steatite) in 1.1, 3, 5, 7.4 and 10 GPa. The kinks are the anomalies at T_c. Upper inset: singular part of the specific heat $C^{electr.}/T$ left after subtraction of a smooth background at 1.1 GPa. Lower inset: pressure dependence of T_c (closed black circles: this work) compared to literature data.[3]

[1] J.W. Loram *et al.*, *J. Phys. Chem. Solids* **59**, 2091 (1998).
[2] T. Timusk and B. Statt, *Report on Progress in Physics* **62**, S. 61 (1999).
[3] J. S. Schilling and S. Klotz, in *Physical Properties of High-Temperature Superconductors, Vol.III*, Ed. D. M. Ginsberg (World Scientific, Singapore, 1992), and references therein.

Missing *d*-wave H_{c2} anisotropy in Y-123

Following the puzzling absence of bulk *d*-wave anisotropy in the specific heat of $YBa_2Cu_3O_7$ for $H\perp c$ (cf. 2003 report), new experiments were initiated, using this time the rotating field given by a split-coil magnet. By avoiding mounting and unmounting the sample between runs, the new experiment should be more significant. The results confirm that only π periodicity is present in the mixed-state specific heat $\gamma(H,\phi)T$ at $T \ll T_c$, whereas the *d*-wave symmetry of the Cooper pairs should introduce a component with $\pi/2$ periodicity (Fig. 9). The measured variation gives

an estimation of the anisotropy of the upper critical field $H_{c2,b}/H_{c2,a}$ = 1.25 associated with the Cu-O chains running along the *b*-axis (the anisotropy $H_{c2,c}/H_{c2,ab}$ is close to 5 for this sample). Unlike surface-sensitive experiments such as tunneling, this bulk test does not support simple views on *d*-wave pairing symmetry in $YBa_2Cu_3O_7$. (Collaboration with C. Meingast, Karlsruhe, and S. Tajima, Tokyo).

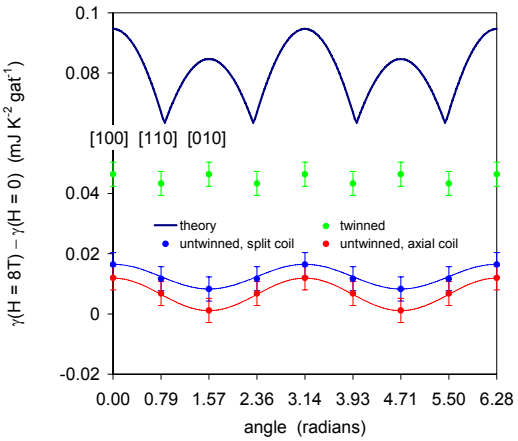

Fig.9. Variation of the coefficient of the linear term of the specific heat $\gamma(H=8\ T,\phi)$ as a function of the angle ϕ between H in the basal plane and the a-axis. Upper curve: calculated dependence for a d-wave orthorhombic superconductor. Green symbols: data for a twinned crystal. Blue and red symbols: data for a detwinned crystal, measured in two experimental conditions. $\gamma(H=0,\phi) \cong 0.21\ mJ\ K^{-2}\ gat^{-1}$.

Nb_3Sn, a two-gap superconductor

Following our finding a second gap in the low-temperature specific heat of the technically applied superconductor Nb_3Sn (cf. 2003 report), experiments of point-contact spectroscopy and tunneling on break junctions were initiated in the group of G. Goll on the same samples. The presence of a second small gap in addition to the main one is confirmed. (Collaboration with G. Goll and W. Goldacker, Karlsruhe).

Development of new types of calorimeters

As new materials are usually available only in small quantities, we developed new types of calorimeters allowing high-resolution measurements of thermal properties of samples with masses of the order of a few milligrams down to a few hundred nanograms.
Most of these calorimeters are based on AC techniques. For example, we built and used modulated-bath calorimeters based on modified Peltier cells in the temperature range from 30 K to room temperature (Fig. 10). In this method, the sample is attached to a thin thermocouple cross, acting as a weak thermal link to a platform; the absence of heater reduces the background heat capacity ("addenda") to a minimum. The temperature of the platform can be modulated periodically by Peltier effect, so that the oscillation is symmetrical about the temperature of the main bath. This avoids the problem of DC offsets which plagues conventional AC calorimeters. For use at temperatures below 30 K where Peltier cooling loses its efficiency, a similar calorimeter using AuFe/chromel thermocouples and Joule heating was developed.

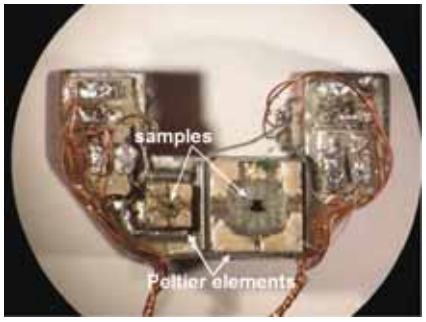

Fig.10. Platform holding two AC calorimeters with their "bath" modulated by Peltier effect. The smaller one, 3.2 x 3.2 mm, uses 25 μm ∅ thermocouples, whereas the larger one, 6.4 x 6.4 mm, uses 50 μm ∅ thermocouples.

Another type of calorimeter combines the advantages of AC calorimetry with those of heat-flow calorimetry (Fig. 11). A thin sapphire disc is suspended to the heat sink by a thermopile made of 24 AuFe/chromel thermocouples. A thin-film Pt heater is deposited onto the platform. The thermopile can either be used as a sensor for AC calorimetry, or measure the heat flow when the temperature of the bath is swept at a constant rate d*T*/d*t*. When working at constant bath temperature while sweeping the magnetic field *H*, it can either give the field dependence of the specific heat with high data density, using AC modulation, or measure the isothermal magnetocaloric effect, using the DC component.
For the measurement of thin-film samples, we finally selected the '3ω'-technique. Test devices using a Pt heater/thermometer deposited onto a Si_3N_4-membrane were realized.

Fig.11. Combined heat-flow and AC calorimeter made of a sapphire disc equipped with a Au-Fe/Chromel thermopile.

Fundamental excitations of correlated matter

Research summary: The group works on the properties of interacting electrons in solids. Prominent examples of unanticipated new phenomena are the fractional quantum Hall effect, high temperature superconductivity, colossal magneto resistance, and quantum phase transitions. The project focuses on physical situations where changes of state of matter take place. Invariably a transition of one state of matter to another is accompanied by a characteristic change of the kinetic energy of the electrons, which can be monitored by measuring the phase stiffness as revealed by the low energy optical spectral weight. Phase transitions are moreover often accompanied by an abrupt change of symmetry at the critical point, and this is revealed optically by the appearance or disappearance of vibrational modes in the infrared range, and by changes of the visible part of the optical spectrum. Ordering phenomena are usually accompanied by the appearance of new collective modes, which in some cases can be detected optically. With this approach we investigate the electronic structure of superconductors in the cuprate and heavy fermion families, Kondo insulators, itinerant ferromagnetic materials and (in)organic one-dimensional materials.

Frequency/temperature scaling in cuprate superconductors

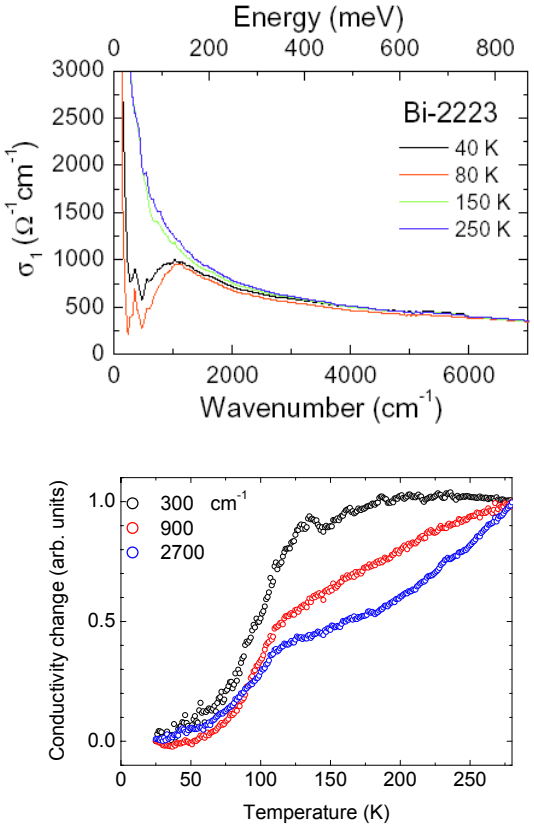

FIG. 1: Dielectric function and optical conductivity of optimally doped Bi2223 as a function of frequency and temperature. The unprecedented detail of the measured temperature dependence permits, among other things, for the first time the analysis of the temperature derivative of the infrared optical constants.

We have extended our studies on two aspects of the ab-plane optical response to a broader range of materials and dopings. These two aspects are the powerlaw behaviour seen in the optimally doped and overdoped samples of Bi2212, and the trends of spectral weight transfer. In particular we have investigated strongly overdoped Bi2212, optimally doped Bi2223, NdBa2CuO6.5, and optimally doped Tl1223. Using an improved setup in the mid-infrared range (0.1 to 1 eV) we have been able to investigate the optical constants with similar temperature and frequency resolution as we have previously obtained for the visible light spectra (H.J.A. Molegraaf *et al., Science* **295**, 2239 (2002); A.B. Kuzmenko *et al., Phys. Rev. Lett.* **91**, 037004 (2003); D. van der Marel *et al., Nature* **425**, 271 (2003)). This has allowed us to follow in unprecedented detail the evolution of the MIR-conductivity as a function of temperature, along with its detailed changes associated with the superconducting phase transition. An example of the temperature and frequency traces for Bi2223 single crystalline material is shown in Fig. 1.

The experimental data are described by the complex valued matrix, $\varepsilon(\omega,T)$, giving the real and imaginary part of the dielectric function for 10'000 frequencies and 260 temperatures. As can be seen from Fig. 1 this allows to identify quite easily the changes associated with the onset of superconductivity. It allows also carrying out a unique and very informative analysis of the normal state: Among other things this has allowed us to verify a suggestion born out by models of quantum critical scaling, that the dielectric function describing the conduction band near optimal doping should to a very good approximation given by an expression of the form

$$\varepsilon(\omega,T)=\frac{1}{\omega^2}\,f\left(\frac{\omega}{T}\right)+\varepsilon_{reg}(\omega),$$

where the first term describes the low frequency response of the charge carriers, which in scenarios of quantum critical behaviour is a

universal function of the frequency devided by the temperature when the sample is tuned exactly to the critical doping or pressure.

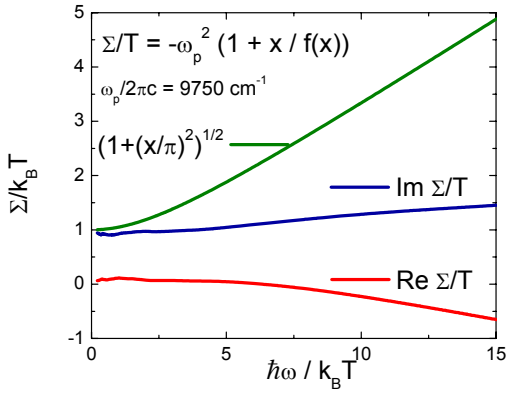

Fig. 2: Scaling function of the optical self energy, where x=ω/T. Clearly the experimental data (blue curve) are quite different from the marginal Fermi-liquid model (olive curve).

The second term, $\varepsilon_{reg}(\omega)$, describes the regular part of the optical response which is not due to quantum criticality, and which represents the contributions coming from interband transitions, optical phonons, etcetera. This term has only a negligible temperature dependence in the infrared range, where $\varepsilon_{reg}(\omega)$ is much smaller than the charge carrier term. A straightforward temperature differential analysis of $d\varepsilon(\omega,T)/dT$ of the experimental data

$$f_{\exp}(\omega,T) = -T\int_0^{\omega} \upsilon \left.\frac{\partial\varepsilon(\upsilon,\tau)}{\partial\tau}\right|_{\tau=T} d\upsilon \quad ,$$

than provides $f_{\exp}(\omega,T)$ directly from the experimental data. This new form of data analysis has the great advantage of eliminating any possible theoretical bias.

The result of the analysis, shown in Fig. 2, confirms that to a very good approximation $f_{exp}(\omega,T) = f(\omega/T)$. It also shows, that to a very good approximation $f(x) = 1/(1+ix^{-1})$. The latter observation contradicts the famous marginal Fermi liquid model of Varma *et al.*, which predicts that $f(x) = 1/\left(1+i\sqrt{1+x^{-2}}\right)$, shown as the olive curves in Fig. 2. The marginal Fermi liquid model is based on the assumption that in the cuprates, near optimal doping, the quasi-particle scattering is characterized by a single energy scale, which is the temperature itself. Of particular relevance are the implications for the notion of quantum critical fluctuations near optimal doping and those for the nature of the electron-electron coupling.

Transition metal silicides

We prepared large clean single crystals of CoSi, and we have measured its infrared optical conductivity as a function of temperature and frequency. Additional studies of the temperature dependent resistivity in an extended temperature range from 4 to 800 K has been carried out for MnSi, FeSi and CoSi. The aim of the latter study is to investigate in more detail the remarkable temperature dependence in MnSi, where it was seen that in the paramagnetic phase above 30 K the resistivity is $\rho = \rho_Q T/(T+T_0)$, where resistivity is $\rho_Q = 280\mu\Omega\text{cm}$, and $T_0 = 180\,\text{K}$ (see FP Mena et al, Phys. Rev. B 67, R241101 (2003)). Our novel data upto 800 K support this result. XAS has been used to study the 3d valence bands, and the local magnetic correlations of MnSi, showing, among other things, strong disagreement between LDA band theory and the experimental data. Theoretical analysis indicates the importance of local Hund's Rule correlations of MnSi.

Optical anisotropy of MgB_2

Magnesium diboride has a strikingly high transition temperature of about 40 K. After 4 years, it still holds an unchallenged record among the 'conventional' BCS-like superconducting metals with a phonon-mediated pairing. The hallmark of MgB_2 is the existence of two very distinct superconducting gaps residing on different sheets of a complicated Fermi surface. Magnesium diboride has yet another 'spectacular' duality: it appears in two colors – gold and silver. We demonstrate with the aid of spectroscopic ellipsometry on high-quality single crystals produced in group of J. Kaprinsky (ETH Zurich) that both colors are intrinsic and stem from rather different electronic responses to the light polarized parallel and perpendicular to the graphite-like boron ab-planes (see Fig. 3). Even though the plasma frequencies along the two directions are very close and correspond to the plasma edge of gold, a strong interband transition for the in-plane polarization at 2.5 eV smears out the plasma edge and makes the 'in-plane color' silver-like. The results are in agreement with the LDA calculations, although the absolute value of the bare electron plasma frequency (5.5 eV) is much lower than predicted by the LDA calculations (6.9 eV). The reason for this discrepancy is a subject of the ongoing research.

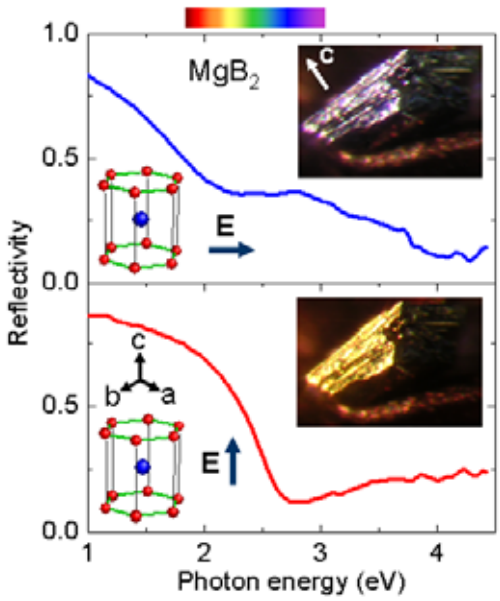

Fig.3 : The reflectivity of single crystal of MgB_2. On the top panel the polarization of the incident light is parallel to the graphite-like boron planes; On the bottom panel it is along the c-axis. The images demonstrate that the sample color depends on the polarization. The gold color (E||c) is caused by a sharp plasma edge at about 2.5 eV. The silver color (E||ab) is due to the flattening of the reflectivity curve in the visible range by a strong interband transition.

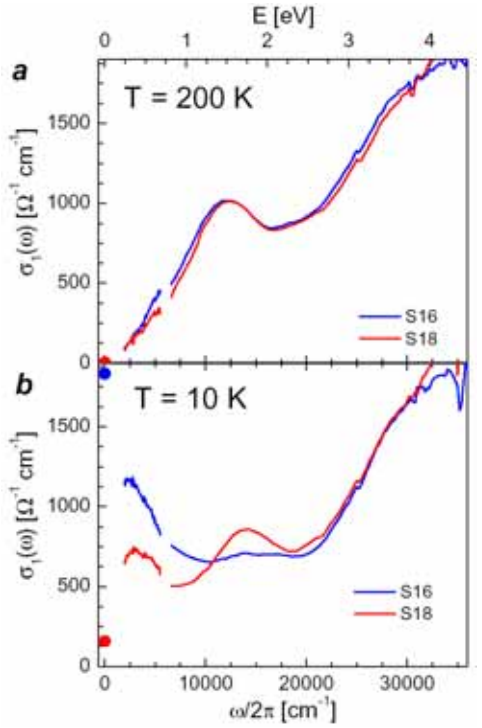

Fig.4 : Oxygen isotope effect on the optical conductivity of $(La_{0.5}Pr_{0.5})_{0.7}Ca_{0.3}MnO_3$ at 200 K (top panel) and 10 K (bottom panel). S16 (blue curves) and S18 (red curves) denote the ^{16}O and ^{18}O samples correspondingly.

Optical study of the oxygen isotope effect in $(La_{0.5}Pr_{0.5})_{0.7}Ca_{0.3}MnO_3$

Few compounds manifest a so ample variety of phases as manganite perovskites do, due to the interaction of charge, spin, orbital and lattice degrees of freedom. One of the most fascinating phenomena is the oxygen isotope effect. For example, $(La,Pr)_{0.7}Ca_{0.3}MnO_3$ is a ferromagnetic metal below ~180 K, but the substitution $^{16}O \rightarrow ^{18}O$ shifts the transition to much lower temperatures and for some compositions may even drive the system to the insulating ground state (N.A.Babushkina et al, Nature, 391, 159). It tells that the interaction with lattice is crucial in the formation of the electronic ground state. Some models predict that the sample becomes phase-separated. We measured optical conductivity of thin epitaxial films of $(La_{0.5}Pr_{0.5})_{0.7}Ca_{0.3}MnO_3$ on $SrTiO_3$ substrate for the two isotope substitutions (Fig. 4).

At 200 K, where both samples are in the insulating phase, the optical conductivity is the same: the Drude contribution is suppressed and the peak at 1.5 eV is well pronounced, which supposedly corresponds to the interatomic transitions with the final spin state of the conducting e_g electron antiparallel to the core t_{2g} spin. Conversely, at low temperatures the isotope substitution drastically changes the spectra for energies up to 2.5-3 eV. The ^{18}O-rich sample has a reduced Drude peak and an increased peak at 1.5 eV, inherent to the insulating phase. The data point toward the separation of the sample into ferromagnetic metallic and paramagnetic insulating domains.

Optical and electronic properties of ZrB_{12}

The discovery of superconductivity in MgB_2 has revived the attention of scientists to other boride compounds. In ZrB_{12}, the zirconium atoms and B_{12} dodecaedra arrange in rock-salt structure (see inset in Fig. 5). The superconductivity at T_c = 6 K in ZrB_{12} has been discovered in the 1960s, but the knowledge of electronic properties was very limited. On large single crystals, grown in the group of Y. Paderno (Kiev), we obtained the optical conductivity of ZrB_{12} (Fig.5) from a combination of high-frequency ellipsometry (above 0.7 eV) and low-frequency reflectivity. We calculated the band structure of ZrB_{12} using full potential LMTO method. The contribution of

interband transitions to the optical conductivity (Fig.2) is in a good agreement with the experimental data. The measured plasma frequency (6.6 eV) also agrees well with the calculated value (6.5 eV). Thus, optics provides an experimental evidence for the validity of the band structure calculations.

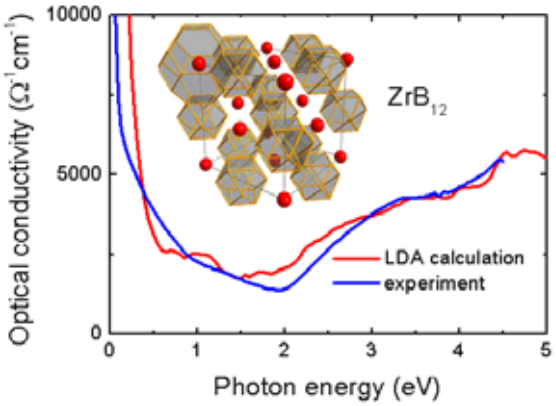

Fig.5 : Optical conductivity of ZrB_{12} computed by from the plasma frequency and the interband transitions (red curve), given by the LDA calculations (convoluted with a Lorenz function to simulate scattering) compared with experimental results (blue curve).

The LDA calculations also show that the substitution of Zr ions with some atoms (Y, Rb) increases the density of states at the Fermi level, which may enhance the superconducting properties. Further experimental and theoretical work is in progress.

Giant magnetocaloric $Gd_5Si_2Ge_2$ compound: optical and photoemission study

The compound $Gd_5Si_2Ge_2$ attracted attention due to its unusually high (giant) magneticaloric effect (4K/Tesla), making it rather promising for the application in cooling devices. The optical properties of $Gd_5Si_2Ge_2$ crystals, fabricated at Ames Lab. (USA), were under investigation. Ellipsometric and reflectivity measurements, ranging from the visible light to the far infrared, allowed us to gain insight into the electronic properties, the magnetic mechanism and the intruigingly high transition temperature of this metallic ferromagnet. At the synchrotron ELETTRA in Trieste, we have additionally performed resonant photo-emission to clarify the contribution of the *5d* Gd electrons to the magnetism.

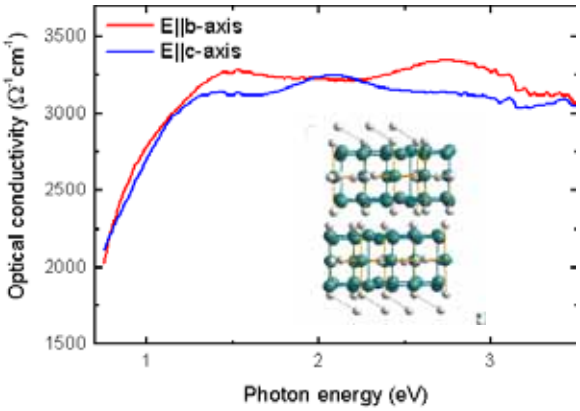

Fig. 6. The anisotropic optical conductivity as obtained from ellipsometric measurements. In the inset, the layered $Gd_5Si_2Ge_2$ structure in the ferromagnetic phase is shown.

CDW formation in $Lu_5Ir_4Si_{10}$

In $Lu_5Ir_4Si_{10}$ the charge transport is realized mainly due to lutetium chains. The nesting condition is nearly satisfied, giving rise to the formation of the charge-density wave (CDW) at 83 K. The transition is clearly observed in the optical spectra, that we measured from 0.08 to 4.5 eV. In the future we plan to do optical measurements, applying pressure up to 21 kBar, when the CDW is suppressed, and simultaneously the superconducting temperature is increased from 3.8 to 9.1 K, displaying the strong interplay between CDW and superconducting order.

Growth and electronic properties of unconventional metals and oxides

Research summary: Unconventional metals and oxides, including dielectric and ferroelectric insulators, ferromagnetic metals, and superconductors, are studied using standard transport, local probes, and high pressure techniques. The materials investigated include single crystals, epitaxial thin films, and heterostructures. Epitaxial ferroelectric films are used to study finite size effects. Ferroelectric domain manipulation and domain wall motion, as well as novel devices are studied and realized using atomic force microscopy. Heterostructures of ferroelectric perovskites with superconducting or metallic oxides allow the realization of local field effect experiments using the nonvolatile ferroelectric polarization field, while ferroelectric / dielectric structures are used to design novel materials with tailored properties. High pressures are used to tune the electronic properties of correlated electron systems, in particular close to phase transitions.

Jean-Marc Triscone

Ferroelectricity and tetragonality in ultrathin $PbTiO_3$ films.

The question of finite size effects in ferroelectrics or, in other words, the question of whether or not there is a critical thickness below which ferroelectricity disappears is still open.

In this study, a series of epitaxial perovskite films of c-axis oriented $PbTiO_3$ ranging from 500 down to 24Å (6 unit cells) were grown using off-axis RF magnetron sputtering onto metallic (001) Nb-$SrTiO_3$ substrates. The thickness of the films, the c-axis length, and the epitaxial growth were studied using high resolution x-ray measurements. As can be seen on Fig. 1, the c-axis parameter systematically decreases with decreasing film thickness below 200Å. Using a first-principles model Hamiltonian approach, the decrease in tetragonality is related to the reduction of polarization. The shortening of the c-axis observed in thin films thus reflects the progressive decrease of the polarization. This important result has been confirmed by XPD measurements performed with P. Aebi in Neuchâtel and extended to thinner films as shown on Fig. 1. These data suggest that films thicker than about three unit cells are ferroelectric and that the progressive polarization reduction is due to the depolarizing field resulting from imperfect screening.

*For more details and further reading, see [1] Junquera et al., Nature **422**, 506 (2003), [2] Lichtensteiger et al., Phys. Rev. Lett. **94**, 047603 (2005).*

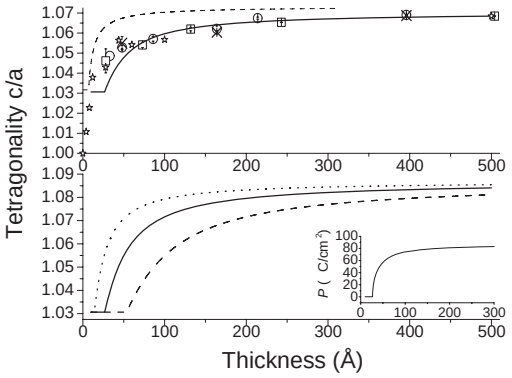

Fig.1. Evolution of the c/a ratio with the film thickness. Top: x-ray experimental results for the 1st series (circles), the 2nd series (squares), and the 1st series with a gold top electrode (crosses); XPD data (stars); the dashed line is the phenomenological theory prediction supposing a ratio between the extrapolation and the correlation length δ/ξ=1.41 (see Ref. [2]); the solid line is the model Hamiltonian prediction for λ_{eff}=0.12Å, rescaled to give a maximum tetragonality in agreement with the experimental data. Bottom: results from the model Hamiltonian calculations for λ_{eff}=0.23Å (dashed line), λ_{eff}=0.12Å (solid line) and λ_{eff}=0.06Å (dotted line). Inset: thickness dependence of the spontaneous polarization P from the model Hamiltonian for λ_{eff}=0.12Å.

Ferroelectric domain wall roughness

Understanding the mechanisms that control domain wall pinning and propagation in ferrolectric materials is of both applied and fundamental interest. Previous studies have shown subcritical domain wall motion to be a creep process, controlled by disorder [1,2].

However, questions about the microscopic nature of the disorder were left open by the dynamic measurements alone, and the possible role of long range dipolar interactions was not addressed. These can be accessed by a direct analysis of the static domain wall roughness, extracting the roughness exponent ζ and the effective domain wall dimensionality d_{eff}. The static configuration of ferroelectric domain walls was investigated using atomic force microscopy (AFM) on epitaxial $PbZr_{0.2}Ti_{0.8}O_3$ thin films. Linear domain structures like those shown in Fig 2, were written with alternating negative and positive voltage signals applied between the metallic AFM tip and the conducting Nb:$SrTiO_3$ substrate. From high resolution piezoresponse

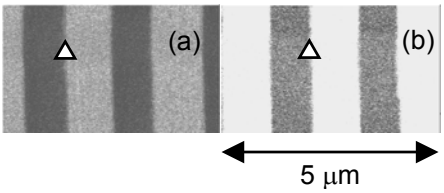

Fig.2. The same set of domain walls imaged (a) 1 hour after writing and (b) 1 week later. The white triangle indicates the same domain wall in each image.

images of the individual domain walls we extracted the correlation function of relative displacements $B(L) = \langle\langle [u(z+L) - u(z)]^2 \rangle\rangle$ where the displacement vector $u(z)$ measures the deformation of the domain wall from an elastically ideal flat configuration due to pinning in energetically favorable regions of the potential landscape, and <<…>> denotes the thermodynamic and ensemble disorder averages. As shown in Fig. 3, we observe a power law growth of $B(L)$ at short length scales, comparable to the 50-100 nm thickness of the films used for these studies, followed by a saturation of $B(L)$ in the 100-1000 nm^2 range which indicates that the domain walls do not relax at large length scales from their initial straight configuration, dictated by the position of the AFM tip during writing.

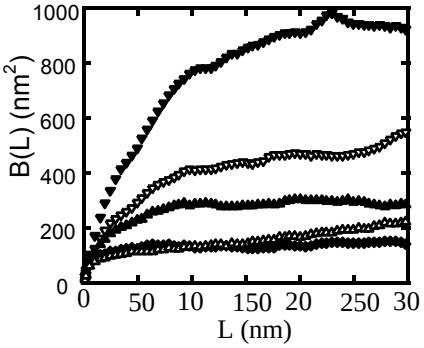

Fig.3. Average displacement correlation function B(L) for different sets of domain walls in a 91 nm thick film.

From the power-law growth of $B(L)$ at short length scales we extract average values of $\zeta \sim$ 0.26, 0.29 and 0.22 for the 50, 66 and 91 nm thick films studied. Independent measurements of domain wall creep in the same samples give values of 0.59, 0.58 and 0.51, respectively, for the dynamical exponent μ.. In the theoretical framework of elastic disordered systems, these two exponents are directly related via $\mu = (d_{eff}-2+2\zeta)/(2-\zeta)$, allowing the effective dimensionality of the films to be obtained as 2.42, 2.49 and 2.47, respectively [3], in very good agreement with the expected theoretical value for a two-dimensional elastic interface in the presence of random-bond type disorder and dipolar interactions.

*For more details and further reading, see [1] Tybell et al., Phys. Rev. Lett. **89**, 097601 (2002), [2] Paruch et al., cond-mat/0411178, [3] Paruch et al., cond-mat/0412470, to appear in Phys. Rev. Lett.*

The unusual behavior of ferroelectric polarization in $PbTiO_3/SrTiO_3$ superlattices

The construction of artificial ferroelectric superlattices with fine periodicity presents exciting possibilities for the development of new materials with extraordinary properties and furthermore a probe for understanding the fundamental physics of ferroelectric materials.

The $PbTiO_3/SrTiO_3$ superlattice system suggests itself as a useful model system for studying the depolarization field effect in $PbTiO_3$ as one expects that similar behavior will be observed in superlattices as in thin films when the relative thickness of the $PbTiO_3$ layers is reduced with respect to the thickness of the $SrTiO_3$ layers. We thus deposited several superlattices of $PbTiO_3/SrTiO_3$ on conducting (001) 0.5% Nb doped $SrTiO_3$ using off axis RF magnetron sputtering.
In the principle series of interest we grew superlattices consisting of 20 $PbTiO_3/SrTiO_3$ bilayers in which the $SrTiO_3$ layer thickness was maintained at 3 unit cells while the $PbTiO_3$ layer thickness was varied from 55 unit cells down to just one unit cell. As discussed above, the $PbTiO_3$ lattice parameter reflects the polarization in the film. Here, the average lattice parameter was used as a probe of the ferroelectric polarization of the superlattice. For thick $PbTiO_3$ layers, the films clearly possess a ferroelectric polarization. When reducing the $PbTiO_3$ layer thickness, the polarization decreases to the point where, for the 3-3 superlattice, the average lattice parameter coincides with that expected for the paraelectric structure. However, the 1 - 3

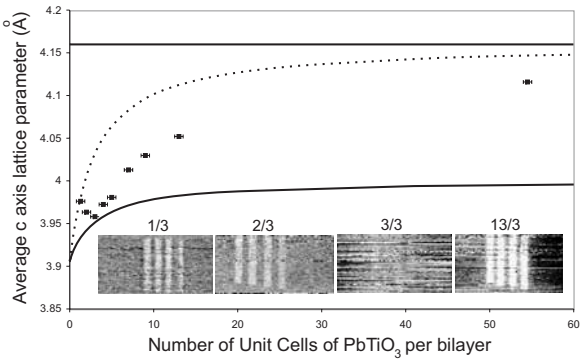

Fig.4. Average c-axis lattice parameters measured by x-ray diffraction and complementary piezoelectric AFM images showing the suppression and recovery of ferroelectricity as the $PbTiO_3$ volume fraction of the superlattice is reduced. The lower solid line represents the expected lattice parameter of a paraelectric sample, while the dotted line represents the volume average of fully ferroelectric $PbTiO_3$ and paraelectric $SrTiO_3$.

and 2 - 3 superlattices surprisingly display larger average lattice parameters that indicate the samples should be ferroelectric. This was confirmed by using piezoelectric AFM to write stripes using alternatively positive and negative voltages as shown on Figure 4.

Transport properties of reduced $SrTiO_3$ single crystal surfaces.

Doped or reduced $SrTiO_3$ displays a metallic behavior and becomes superconducting at very low temperatures (<0.5K). In addition, its superconducting critical temperature depends strongly on the carrier concentration, making this material very attractive for field effect experiments. We have used a hydrogen plasma cleaning procedure to reduce the surface of $SrTiO_3$ (STO) single crystal substrates. This procedure allows us to obtain a metallic superficial layer, whose thickness is however *a priori* unknown. Many experiments show that the samples resistance values increase as a function of time. However, a remarkable scaling of the normalized resistivities, ρ(T)/ρ(296K), for different samples and for different "waiting time" is observed. Only at low temperatures, a change in behavior is measured for different plasma reduction conditions. A substantial magnetoresistance is also seen to develop below about 100K, a result in agreement with our measurements on Nb-doped STO discussed in detail below. Hall effect test measurements have also been performed and the carriers mobility has been deduced.

Electrostatic modulation of the electronic properties of Nb-doped $SrTiO_3$ superconducting films.

We have performed ferroelectric field effect experiments using epitaxial heterostructures composed of ferroelectric $Pb(Zr_{0.2}Ti_{0.8})O_3$ and superconducting Nb-doped $SrTiO_3$ (Nb-STO). The films were prepared on (001) $SrTiO_3$ substrates by off-axis radio-frequency magnetron sputtering and pulsed-laser deposition. To switch the direction of the ferroelectric polarization (parallel (P+) or anti-parallel (P-) to the c-axis), the metallic tip of an AFM was used as a mobile gate electrode, scanning at room temperature over the whole area of the conducting path.
Figure 5 shows the temperature dependence of the resistance for the P+ and P- states and the resistance difference ratio between the two states. In the temperature range investigated, both states display a metallic behavior and a large resistance change between the two states is observed. The inset of Fig. 5 shows the resistivity behavior below 0.4 K and down to 0.15 K. For the two polarization states, a narrow superconducting transition is observed with the resistivity reaching zero within the experimental resolution and a clear shift of T_c is observed. With T_c defined as the temperature at which the resistivity decreases to 50 % of its value at 0.4 K, the T_c value for the P- state is 0.30 K and that of the P+ state is 0.24 K (a 20 % change). As shown by the green arrow, in a temperature range around 0.27 K, switching of the ferroelectric polarization induces a remarkable transition from the normal metallic state (P+ state) to the superconducting zero resistance state (P- state).

In order to quantify the electrostatic modulation of the carrier density, the Hall effect was measured at various temperatures for the two polarization states.

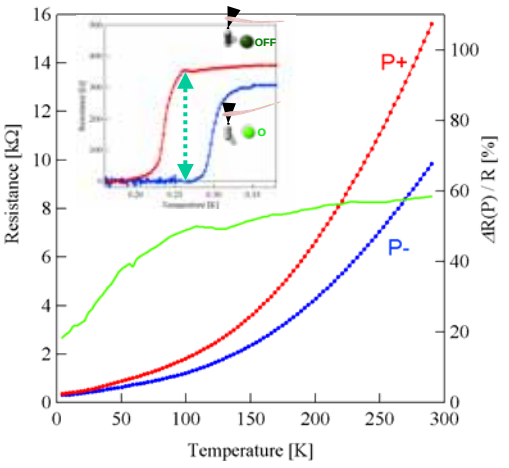

Fig.5. Left axis: Resistance versus temperature (for the two polarization states). P+ corresponds to the polarization direction that removes electrons from the Nb-STO layer. In the P- state, the polarization field adds electrons to the film, lowering the resistance. Right axis: (green curve) : Temperature dependence of the resistance difference ratio between the two polarization states defined as ΔR(P)}{R} ={R (P+) - R (P-)}/R (P-). The inset shows the resistance at low temperatures. The superconducting on-off non-volatile reversible ferroelectric switching is realized around 0.27 K as illustrated by the green arrow.

Figure 6 shows the inverse Hall coefficient (R_H^{-1}) for the P+ and P- states and the difference, ΔR_H^{-1}, as a function of temperature. Below 100 K, R_H^{-1} decreases dramatically for both polarization states as does ΔR_H^{-1}, which drops from $\Delta R_H^{-1} = 4.5 \times 10^6$ C/m^3 at high temperatures to 0.35×10^6 C/m^3 below 25 K.
In a simple picture, one would expect R_H^{-1} and ΔR_H^{-1}, the difference in carrier concentration (proportional to Δn), to remain essentially constant as the temperature is decreased (the ferroelectric polarization being essentially constant below room temperature). This is in sharp contrast with the dramatic decrease

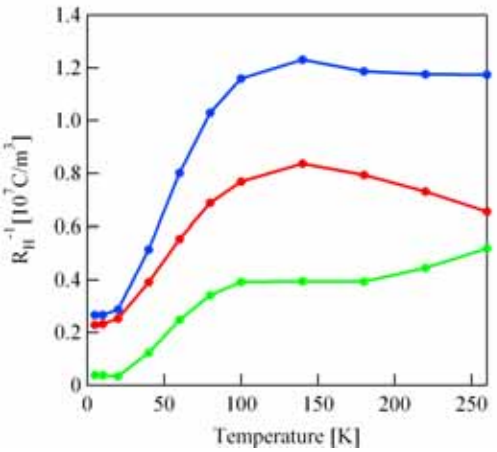

Fig.6. Temperature dependence of the inverse Hall constant (R_H^{-1}) for each polarization state (blue and red curves) and the difference in inverse Hall constants (ΔR_H^{-1}).

observed below 100K for R_H^{-1} and ΔR_H^{-1}. Although the origin of this anomalous temperature dependence is not completely clear, we think that this behavior reflects the physics of doped $SrTiO_3$ and the presence of different types of carriers which may originate from the two bands known to contribute to transport in doped $SrTiO_3$ or to the field induced carrier profile.

Quantification of the induced charge density in field effect experiments

The density of mobile holes governs the electronic transport properties of high-T_c superconductors. This quantity can be chemically controlled by doping, giving rise to the generic temperature versus doping level phase diagram. The electrostatic field effect technique allows only the carrier density of these systems to be changed without affecting other parameters like the disorder. In this work we show that we are able to induce T_c modulations of several Kelvin in thin $NdBa_2Cu_3O_{7-\delta}$ (NBCO) films for induced charge densities of the order of $0.7*10^{14}$ charges/cm^2 using a field effect device based on a $SrTiO_3$ (STO) single crystal used as a substrate and as a gate dielectric. We principally used commercial substrates, 100 μm thick. The superconducting NBCO thin film is first grown on the 100 μm thick STO substrate and then protected by an amorphous NBCO layer deposited in-situ. After the deposition, the sample is photolithographically patterned using ion milling and a gold electrode is deposited on the back of the sample and positioned at the back of the superconducting path. During the measurements, gate leakage currents were kept below a few nA. In order to correlate the field-induced changes in the critical temperature of

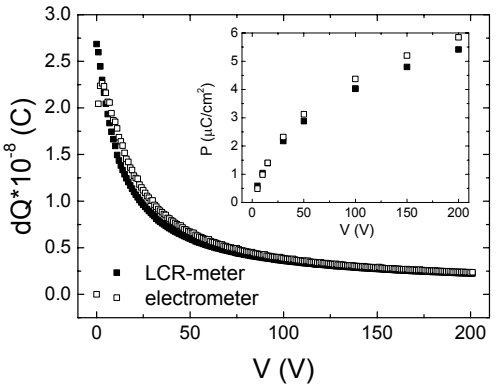

Fig.7. dQ(V)=C(V)dV measured by an LCR-meter and by an electrometer at each voltage V for a 100 μm thick STO substrate at 4.2 K. Inset: The corresponding field induced charge density σ(V) at a given voltage is calculated by integrating the charge measured by the electrometer and the LCR-meter.

thin NBCO films with the field-induced carrier density, we determine the accumulated charge on the devices. As the dielectric constant of STO depends on temperature and applied electric field, the polarization of the device has to be measured at each temperature and for each applied electric field. Measurement of the induced charge density σ at a given temperature is done by measuring the capacitance of the device as a function of the applied voltage using an LCR meter (model Agilent 4284A) with an auto-balancing bridge method and by measuring the charge flow during loading using a Keithley electrometer.

The field induced charge dQ=C(V)dV measured using the two independent methods is compared in Fig.7 for a 100 μm thick STO substrate with two parallel 20 mm^2 square gold electrodes at 4.2 K. By ramping the voltage across the dielectric, the LCR-meter measures the "local" capacitance C(V) at a given voltage while the electrometer measures dQ, the change in charge for a given change in voltage. On Fig. 7 dQ(V) is plotted as a function of V and the two measurements are in good quantitative agreement. The inset of Fig. 7 shows the corresponding field induced charge density σ(V) at a given voltage calculated by integrating the curves of Fig. 7 and giving similar results for the two experimental methods. To compare T_c changes in four different NBCO thin films, we define T_c as the temperature at which ρ=0.4 μΩcm. Fig. 8 shows the absolute change in T_c as a function of the measured surface field-induced charge density (Δn).

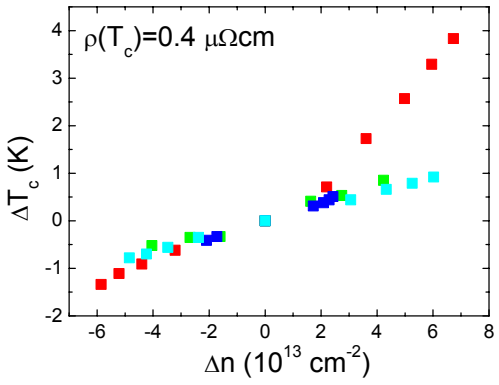

Fig.8. Absolute change in T_c for four different NBCO thin films 3.6 nm (red, green and cyan points) and 5 nm (blue points) thick as a function of the measured field-induced charge density.

The blue points correspond to a 5 nm thick NBCO film while the red, green and cyan points correspond to 3.6 nm thick NBCO films. An overlap of the T_c curves as a function of Δn is observed on Fig 8. An asymmetry between the + and – polarity is also observed for one of the samples. Trapping states at the interface in a given sample may affect the observed amplitude in a field effect experiment and may be a possible explanation for the different behaviors observed on Fig. 8.

New questions on the unconventional superconductivity of iron around its critical pressure

The discovery of superconductivity (SC) in pure iron at high-pressure (K. Shimizu *et al.*, Nature **412** (2001) 316) arrived as something not completely unexpected: indeed, it had been postulated by Wolfarth in 1979 that a superconducting state could develop in non-magnetic ε-iron. However, it soon became evident that a conventional scenario of phonon-mediated pairing could not be invoked to explain several observations, such as the narrow pressure-range (*P* between 13-30 GPa) in which SC is observed. Transport measurements showed that disorder scattering, probed by the residual resistivity ratio (RRR), is a key parameter, while cold-working has a strong pair breaking effect. Indeed, SC can be recovered by proper annealing. The strong influence of ferromagnetic (FM) spin fluctuations on the normal state resistivity ($\rho \propto AT^{5/3}$, with a largely enhanced *A* coefficient) and their relation to SC (*A* mimics the pressure-dependence of the SC critical temperature, T_c) suggest magnetism as a possible pairing mechanism (A. T. Holmes *et al.*, J. Phys.: Condens. Matter **16** (2004) S1121). Pure iron is thus an excellent candidate to study the interplay of ferromagnetism and superconductivity.

We have extended our study of the SC-pocket in iron to higher pressures, by performing accurate resistivity measurements in high-purity Fe-whiskers down to 35mK. The whiskers were grown in the laboratory of Y. Onuki at Osaka, Japan. To achieve the desired higher pressures, the flat part of the sintered diamond anvils was reduced to 1.5 mm.

We have determined the evolution of T_c in one order of magnitude as it decreases towards the critical pressure P_c. Our data for T_c onset (closed circles in Fig. 9) can be fitted to a function of the form $T_c \propto (P_c\text{-}P)^n$, giving $P_c \approx 31$ GPa and $n \approx 0.7$. We have also shown that above the entire SC-region the anomalous *T*-dependence in the resistivity ($\rho \propto AT^{5/3}$) holds for $T>T_c$ up to rather large temperatures ($T > 50$K), showing the robustness of this near-FM state. Unexpectedly, the Fermi liquid regime ($\rho \propto T^2$) is still not recovered at the highest investigated pressure of 30.5 GPa (which is our record pressure) where T_c vanishes.

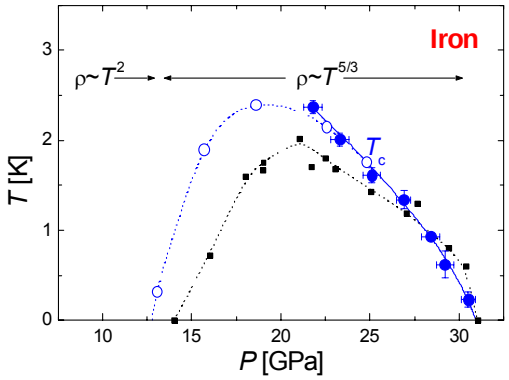

Fig.9. Phase diagram of iron around its superconducting pocket. Our new T_c data are plotted along with previous ones from polycrystals and the data from K. Shimizu et al. (black square).

Two striking features observed in our measurements open new questions on this subject. The first concerns the large reduction of T_c in comparison with a drop of only 50% in the *A*-coefficient. In a scenario where the coefficient *A* is an indirect measure of the superconducting coupling, this seems to indicate the existence of a threshold value of *A* for superconductivity. The second feature is that, with the vanishing of T_c, the SC transition involves a decreasing portion of the sample (measured by the drop in $\rho(T)$ at the transition) despite an increasing RRR. This may point to the martensitic character of the α-ε first-order transition of iron and suggests new experiments in better pressure-homogeneity conditions.

For more details and further reading, see D. Jaccard and A. T. Holmes, cond-mat/0410143.

Below we summarize more briefly other ongoing activities.

High density arrays of ferroelectric domains in thin $Pb(Ti_{0.2}Zr_{0.8})O_3$ films

To achieve high density ferroelectric arrays, we quantitatively studied the piezoelectric response of PZT thin films. We determined the piezoelectric coefficient along the c-axis (d_{33}), using the AFM to measure the piezoresponse amplitude as a function of the amplitude of the signal applied to the tip. To increase the measurement area, a Au electrode was deposited on top of the film and maintained at the same voltage as the AFM tip in contact with it. Depending on the electrical configuration chosen (tip or substrate grounded), d_{33} values ranging between 25 and 45 pm/V were found, compared to a standard value of about 50 pm/V for bulk samples. A typical measurement is shown on Fig. 10.

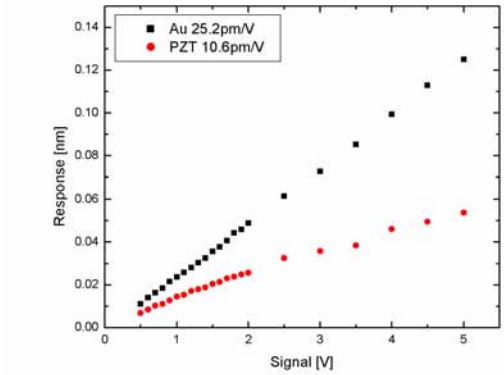

Fig.10. Response of the AFM to application of an alternative voltage on the substrate. The signal is applied on the Au electrode for the upper curve and directly on PZT for the second one.

Using a sample with optimized ferroelectric and piezoelectric properties, we created arrays of circular domains (dots) by moving the tip to predefined position on the film and applying voltage pulses. In order to illustrate the precision of such AFM control of the polarization, we wrote the word "MaNEP" by leaving positions unwritten in an array of 28 x 11 dots (Fig. 11).

Fig.11. Array of 28x11 dots showing the word "MaNEP". The density is about 6Gbit/cm^2.

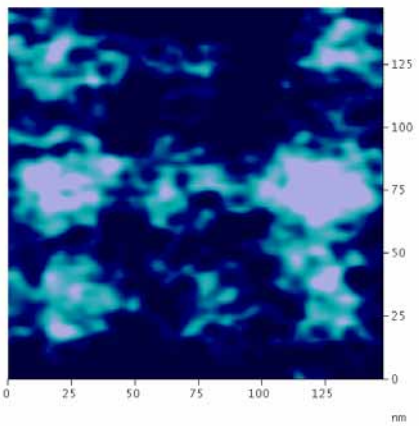

Fig.12. Array of 3x3 dots with a density of 40 [Gbit/cm^2].

Domains with radii as small as 19 nm could also be created allowing us us to achieve densities as high as 40 Gbit/cm^2 as illustrated on Fig. 12.

Electrostatic modulation of the critical current in HTS Josephson Junctions

Here we investigated the electric field effect on the properties of both normal and superconducting states of $NdBa_2Cu_3O_7$ (NBCO) thin films. NBCO films were grown on bicrystalline $SrTiO_3$ (STO) substrates by RF magnetron sputtering. The bicrystal that we used is composed of two fused single crystals with the same *c*-axis direction, but different directions of the *a* and *b* axes. At the boundary between the two crystals, one can obtain a Josephson junction (JJ). Indeed, for the 24° misalignement of our bicrystal, the crystalline order of STO is destroyed over a width of about 1.5nm, which is on the order of the coherence length of the NBCO. Figure 13 shows the current versus bias curves (IV curves) of one of our junction, with a typical JJ-behaviour.

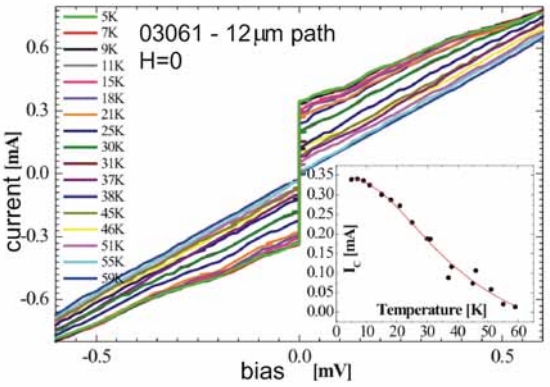

Fig.13. The typical I-V curves of a JJ observed for one of our samples. The inset show the critical current versus temperature.

In order to apply an electric field, we used the back of the STO substrate (which is covered by silver paste) as an electrode and the film itself as the second electrode. In a 75 nm thick NBCO film we obtained a variation of the critical current as high as 12%, for an applied bias of up to 150 V (see figure 14). This effect correspond to a variation of about 1.2 $\mu A/(\mu C/cm^2)$.

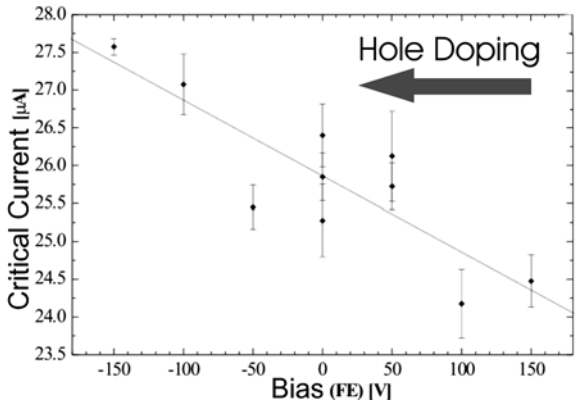

Fig.14. Field effect on one of our Josephson junctions. There is a critical current variation of about 12% between –150V and +150V bias.

Nernst effect in underdoped $NdBa_2Cu_3O_{7-x}$ thin films

We started a study of the Nernst effect together with other transport properties (Hall and Seebeck effects) in order to better understand the origin of the anomalous Nernst signal in the pseudogap state. Our measurements were carried out on single crystal $NdBa_2Cu_3O_{7-x}$ thin films having different oxygen dopings. The samples were grown on (001) $SrTiO_3$ single crystals by off-axis radio-frequency magnetron sputtering. All films were epitaxial with the c-axis perpendicular to the substrate surface. The sample thickness varied between 70 and 80 nm. We measured one optimally doped sample with a zero magnetic field critical temperature T_c of 88.5 K, corresponding roughly to x = 1, and three underdoped samples with T_cs (approximate dopings) of 58.8 K (x = 0.7), 22 K (x = 0.47) and 17 K (x = 0.46). In order to avoid any unwanted contributions from other effects, the Nernst coefficient has been anti-symmetrized and the thermopower symmetrized with respect to the magnetic field. The Hall effect has been anti-symmetrized with respect to both the magnetic and the electric field. The set of measurements allows us to establish a temperature versus doping phase diagram (Fig. 15) correlating the characteristic temperatures of the different transport properties.

T^*_{Nernst} denotes the temperature below which the Nernst coefficient starts to increase in the pseudogap state, T^*_{Hall} is the temperature below which the inverse Hall coefficient is no longer linear in temperature and $T^*_{Seebeck}$ denotes the maximum in the thermopower. T^*_{Hall} and $T^*_{Seebeck}$ can be associated with the opening of the pseudogap.

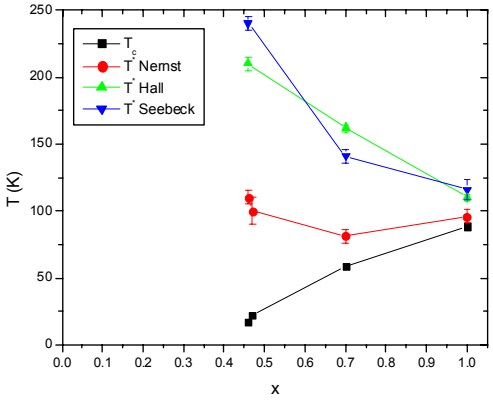

Fig.15. Temperature versus doping (x) phase diagram.

Fig. 15 shows that T^*_{Nernst} is only weakly doping-dependent and not correlated with T^*_{Hall} and $T^*_{Seebeck}$. This behavior is in sharp contrast to results found in $La_{2-x}Sr_xCuO_4$ and $Bi_2Sr_{2-y}La_yCuO_6$ crystals, where T^*_{Nernst} increases with decreasing doping for moderately underdoped samples. We also found that the Hall and Seebeck effects do not show any signature at T^*_{Nernst}. The sensitivity of the Nernst effect to fluctuations suggests that the Nernst signal above T_c is related to superconducting fluctuations.

Selected references:

"Electrostatic modulation of the electronic properties of Nb-doped $SrTiO_3$ superconducting films".
K. Takahashi, D. Matthey, D. Jaccard, J.-M. Triscone, K. Shibuya, T. Ohnishi, and M. Lippmaa.
Applied Physics Letters **84**, 1722 (2004).

"Ferroelectricity and tetragonality in ultrathin $PbTiO_3$ films".
C. Lichtensteiger, J.-M. Triscone, J. Junquera, and P. Ghosez.
Physical Review Letters **94**, 047603 (2005).

"Domain wall roughness in epitaxial ferroelectric $PbZr_{0.2}Ti_{0.8}O_3$ thin films".
P. Paruch, T. Giamarchi, and J.-M. Triscone.
cond-mat/0412470 / To appear in Physical Review Letters.

"Signatures of valence fluctuations in $CeCu_2Si_2$ under high pressure".
A. T. Holmes, D. Jaccard., K. Miyake.
Phys. Rev. B **69**, 024508 (2004).

Collaborations

Dr. M. Abplanalp
ABB Research Center, Baden-Dättwil, Switzerland

Prof. P. Aebi
Université de Neuchâtel, Switzerland

Dr. G. Aeppli
Dept. of Physics and Astronomy,
University College London

Prof. C.H. Ahn
Yale University, USA

Prof. N. Andrei
Rutgers University, USA

Dr. S. Ballandras
LPMO, Besançon, France

Dr. B. Barbiellini
Northeastern University, Boston, USA

Dr. G. Behr
Institute for Solid State and Materials Research, Dresden, Germany

Dr. C. Beneduce
Bruker Biospin SA, Fällanden, Switzerland

Dr. H. Berger
IPMC, EPF Lausanne, Switzerland

Dr. N. Binggeli
Abdus Salam International Center for Theoretical Physics and INFM DEMOCRITOS National Simulation Center, Trieste, Italy

Prof. P. Buffat
EPF Lausanne, Switzerland

Prof. D. Caplin
Imperial College, London, GB

Dr. M.A. Cazalilla
Donostia Center, Spain

Dr. R. Citro
University of Salermo, Italy

Dr. M. Dhallé
Technische Natuurwetenschappen
University of Twente
Enschede, The Netherlands

Prof. M. Di Ventra
University of California, San Diego, La Jolla, USA

Prof. D. Dominguez
Centro Atomico, Bariloche, Argentina

Prof. M. Dressel
University of Stuttgart, Germany

Dr. S. B. Dugdale, M. A. Alam
University of Bristol, UK

J. Duron, F. Grilli
EPF Lausanne, Switzerland

Dr. B. Dutoit
EPF Lausanne, Switzerland

Dr. D. Eckert
Bruker Biospin SA, Fällanden, Switzerland

Prof. C.B. Eom
University of Wisconsin-Madison, USA

Dr. D. Eshchenko, Dr. R. Krasov,
Dr. E. Morenzini, PSI

Dr. M.R. Eskildsen
Notre Dame University, IN, USA

Dr Ph. Fluckiger, Dr. G.-A. Racine
CMI, EPFL, Lausanne, Switzerland

Prof. J. Flouquet
CENG, Grenoble, France

Dr. J. Fompeyrine, Dr. J.-P. Locquet
IBM Rüschlikon, Switzerland

Prof. L. Forro
EPF Lausanne, Switzerland

Prof. A. Furrer, Dr. K. Conder
Laboratory for neutron scattering, ETH Zürich
and PSI Villigen, Switzerland

Prof. V. Gasparov
Institute of Solid State Physics, Russian Academy of Sciences, Chernogolova, Russia

Dr. C. Geibel
MPI, Dresden, Germany

Dr. A. Georges
Ecole Polytechnique, Paris, France

Prof. P. Ghosez
Univ. of Liège, Belgium

Prof. R.E. Gladyshevskii
Dept. of Inorganic Chemistry
Ivan Franko National University, L'viv, Ukraine

Dr. W. Goldacker
Institut für Technische Physik, Forschungszentrum Karlsruhe, Germany

Dr. G. Goll
Physikalisches Institut, Universität Karlsruhe, Germany

Dr. G. Grasso
INFM Genoa, Italy

Dr. D. Grempel
CEA, Paris, France

Prof. M. Greven
Stanford University, Dept. of Applied Physics and
Stanford Synchrotron Radiation Laboratory
Geballe Laboratory for Advanced Materials

Dr. M. Grioni
EPFL, Lausanne, Switzerland

Dr. J.-C. Grivel
Risø National Laboratory, Roskilde, Denmark
Dr. B. ten Haken
Technical University Twente, Enschede,
The Netherlands

Dr. A.F. Ho
University of Birmingham, UK

Dr. B.W. Hoogenboom
Université de Bâle, Switzerland

Dr. Y.-B. Huang
American Superconductor, Westborough, MA, USA

Prof. H. Hwang
TIT, Tokyo, Japan

Prof. J.L. Jorda and Dr. Ph. Galez
Laboratoire de Structure de la Matière,
Université de Savoie, Annecy, France

Dr. I. Joumard
ESRF, Grenoble, France

Dr. J. Karpinski
Laboratorium für Festkörperphysik, ETH, Zürich,
Switzerland

Prof. H. ten Kate
CERN, Geneva, Switzerland

Prof. M. Kawasaki
Tohoku University, Japan

Prof. H. Keller
Universität Zürich, Switzerland

Prof. P. Komarek and Dr. W. Goldacker
Forschungzentrum Karlsruhe, Germany

Dr. A.A. Kordyuk
Institute for Solid State Research, IFW Dresden,
Germany
Institute of Metal Physics of the National Academy of
Sciences of Ukraine, Kyiv, Ukraine

Dr. W. Krauth
ENS, Paris, France

Prof. D.C. Larbalestier
University of Wisconsin, Madison, USA

Dr. P. Le Doussal
ENS, Paris, France

Prof. M. Lippmaa
University of Tokyo, Japan

Dr. C. Meingast, Dr. T. Wolf
Institut für Festkörperphysik, Forschungszentrum
Karlsruhe, Germany

Dr. J. Mesot
Laboratory for Neutron Scattering
ETH Zürich & PSI Villigen, Switzerland

Prof. K. Miyake
University of Osaka, Japan

Prof. Y. Onuki
Osaka, Japan

Dr. E. Orignac
ENS, Paris, France

Dr. Yu. Paderno
Institute for Problems of Materials Science, Academy
of Sciences of Ukraine, Kiev, Ukraine

Prof. F. Parmigiani
Elletra, Trieste, Italy

Dr. M. Potel, Dr. R. Chevrel
Université de Rennes, France

Prof. K.M. Rabe
Rutgers Univ, N.J., USA

Prof. M. Rappaz
EPF Lausanne, Switzerland

Dr. A. Revcolevschi
Laboratoire de Physico-Chimie des Solides
Université Paris-Sud, Orsay, France

Dr. G. Santi
University of Aarhus, Denmark

Dr. J. Sarrao
Los Alamos National Laboratory, N.M., USA

Dr. G. Schehr
University des Saarlandes, Germany

Prof. J. S. Schilling
Washington University, St Louis, USA

Dr. B. Seeber
Groupe de Physique Appliquée
Université de Genève, Switzerland

Prof. D. Shaltiel
Hebrew University of Jerusalem, Israël

Dr. D. Sheptyakov
PSI, Villigen, Switzerland

Dr. C. Simon and Dr. A. Ruyter
CRISMAT Caen and LEMA Tours, France

Dr. C. Simon and Dr. A. Ruyter
CRISMAT Caen and LEMA Tours, France

Prof. A.S. Siri
University of Genoa, Italy

Prof. S. Tajima, Dr. S. Lee, Dr. T. Masui
Superconductivity Research Laboratory, ISTEC,
Tokyo, Japan

Dr. P. Tixador, Dr. C. Villard
CNRS, CRETA, CRTBT, Grenoble, France

Prof. G. Triscone
Ecole d'Ingénieurs de Genève HES
Genève, Switzerland

Prof. T. Tybell
NTNU, Trondheim, Norway

Prof. R. Vaglio
Univ. de Naples, Italy

Prof. H.W. Weber, Dr. M. Eisterer
Atominstitut der Österreichischen Universitäten,
Vienna, Austria

Dr. F. Weiss, Dr. C. Gimenez
LMPG, Grenoble, France

Dr. H. Wilhelm
Max-Planck Institut, Dresden, Germany

Dr. P. Wochner
MPI Stuttgart, Germany

Prof. J. Zaanen
Lorentz Instute, Leiden University, The Netherlands

Publications

Groupe Fischer

Reymond S. and Fischer Ø. *Low temperature scanning contact potentiometry*. Review of Scientist Instruments **75**, 694-698 (2004).

Reymond S., Antognazza L., Decroux M. and Fischer Ø. *Simulation of the initial response of a high Tc superconducting film submitted to a voltage source*. Supercond. Sci. Technol. **17**, 522-526 (2004).

Groupe Flükiger

Lezza P., Abächerli V., Clayton N., Senatore C., Uglietti D., Suo H.L. and Flükiger R. *Transport properties and exponential n-values of Fe/MgB_2 tapes with various MgB2 particle sizes*. Physica C **401**, 305-309 (2004)

Giannini E., Garnier V., Gladyshevskii R. and Flükiger R. *Growth and characterization of $Bi_2Sr_2Ca_2Cu_3O_{10}$ and $(BiPb)_2Sr_2Ca_2Cu_3O_{10-\delta}$ single crystals*. Supercond. Sci. Technol. **17**, 220-226 (2004).

Musolino N., Bals S., van Tendeloo G., Clayton N., Walker E. and Flükiger R. *Investigation of (Bi,Pb)2212 crystals: observation of modulation-free phase.* Physica C **401**, 270-272 (2004).

Senatore C., Polichetti M., Clayton N., Flükiger R., Pace S. *Non-linear magnetic response of MgB_2 bulk superconductors*. Physica C **401**, 182-186 (2004).

Senatore C., Polichetti M., Clayton N., Flükiger R. and Pace S. *Detection of the vortex dynamic regimes in MgB_2 by third harmonic AC susceptibility measurements*. Focus on Superconductivity, pp 51-68, Editor Barry P. Martins, Nova Science Publisher, Inc., NY, 2003 invited contribution.

Uglietti D., Seeber B., Abächerli V., Pollini A., Eckert D. and Flükiger R. *A device for critical current versus strain measurements up to 1000 A and 17 T on 80 cm long HTS and LTS technical superconductors.* Supercond. Sci. Technol. **16**, 1000-1004 (2003).

Perez R., Rojas H., Wälder G. and Flükiger R. *Theoretical modelling of energy balance in electroerosion*. Journal of Materials Processing Technology **149**, 198-203 (2004).

Musolino N., Clayton N. and Flükiger R. *Vortex phases in modulation-free (Bi,Pb)-2212 Crystals.* Physica C **417**, 40-49 (2004).

Flükiger R. and Giannini E. *Bi,Pb(22223) tapes: present and future*. Scenet Newsletter No **3**, 7-10 (2003).

Clayton N., Musolino N., Giannini E., Garnier V. and Flükiger R. *Growth and superconducting properties of $Bi_2Sr_2Ca_2Cu_3O_{10}$ single crystals*. Supercond. Sci. Technol. **17**, S563-S567 (2004).

Gladyshevskii R., Musolino N. and Flükiger R. *Structural origin of the low superconducting anisotropy of $Bi_{1.7}Pb_{0.4}Sr_2Ca_{0.9}Cu_2O_8$ crystals*. Physical Review B **70**, 184522 (2004).

Fujii H., Garnier V., Giannini E. and Flükiger R. *Effect of hot uniaxial pressing on the microstructure and critical current density of (Bi,Pb)-2223 tapes.* Supercond. Sci. Technol. **17**, 263-268 (2004).

Garnier V., Giannini E., Hugi S., Seeber B. and Flükiger R. *New apparatus for DTA at 2000 bar: thermodynamic studies on Au, Ag, Al and HTSC oxides*. Supercond. Sci. Technol. **17**, 395-400 (2004).

Giannini E., Garnier V., Clayton N., Musolino N., Gladyshevskii R. and Flükiger R. *Growth, structure and superconducting properties of $Bi_2Sr_2Ca_2Cu_3O_{10}$ and $(Bi,Pb)_2Sr_2Ca_2Cu_3O_{10-y}$ crystals*. Cryst. Res. Technol. **39**, No 10, 926-931 (2004).

Cusanelli G., Hessler-Wyser A., Bobard F., Demellayer R., Perez R. and Flükiger R. *Microstructure at submicron scale of the white layer produced by EDM technique*. Journal of Materials Processing Technology **149**, 289-295 (2004).

Groupe Giamarchi

Berthod C. *Vorticity and vortex-core states*. Physical Review B **71**, Art. No.134513 Mar 2005.

Bolech C.J., Giamarchi T. *Keldysh study of point-contact tunneling between superconductors.* Physical Review B **71** (2): Art. No. 024517 (2005).

Bolech C.J., Rosso A. *Universal statistics of the critical depinning force of elastic systems in random media*. Physical Review Letters **93** (12): Art. No. 125701 (2004).

Bolech C.J., Giamarchi T. *Point-contact tunneling involving low-dimensional spin-triplet superconductors* Physical Review Letters **92** (12): Art. No. 127001 (2004).

Dressel M., Petukhov K., Salameh B., Zornoza R.; Giamarchi T. *Scaling behavior of the longitudinal and transverse transport in quasi-one-dimensional organic conductors*. Physical Review B **71** (7): Art. No. 075104 (2005).

Giamarchi T. *Theoretical framework for quasi-one dimensional systems*. Chemical Reviews **104** (11) 5037-5055 (2004).

Giamarchi T., Biermann S., Georges A., Lichtenstein A. *Dimensional crossover and deconfinement in Bechgaard salts*. Journal de Physique IV **114**: 23-28 (2004).

Ho A.F., Cazalilla M.A., Giamarchi T. *Deconfinement in a 2D optical lattice of coupled 1D boson systems.* Physical Review Letters **92** (13): Art. No. 130405 (2004).

Hughes R.J., Dugdale S.B., Major Z., Alam M.A., Jarlborg T., Bruno E., Ginatempo B. *Evolution of the Fermi surface and the oscillatory exchange coupling across Cr and Cr-based alloys*. Physical Review B **69** (17): Art. No. 174406 (2004).

Jarlborg T. *Electronic structure and magnetism for FeSi(1-x)Gex from supercell calculations.* Journal of Magnetism and Magnetic Materials **283** (2-3) 238-246 (2004).

Jarlborg T. *Anti-ferromagnetism, spin-phonon interaction and the local-density approximation in high-T-c superconductors.* Journal of Physics-Condensed Matter **16** (13) L173-L178 (2004).

Kolton A.B., Rosso A., Giamarchi T. *Creep motion of an elastic string in a random potential*. Physical Review Letters **94** (4): Art. No. 047002 (2005).

Kolton A.B., Grempel D.R., Dominguez D. *Heterogeneous dynamics of the three-dimensional Coulomb glass out of equilibrium*. Physical Review B **71** (2): Art. No. 024206 (2005).

Major Z., Dugdale S.B., Watts R.J., Santi G., Alam M.A., Hayden S.M., Duffy J.A., Taylor J.W. Jarlborg T., Bruno E., Benea D., Ebert H. *Direct observation of the multisheet Fermi surface in the strongly correlated transition metal compound ZrZn2.* Physical Review Letters **92** (10): Art. No. 107003 (2004).

Moulinet S., Rosso A., Krauth W., Rolley E. *Width distribution of contact lines on a disordered substrate*. Physical Review E **69** (3): Art. No. 035103 Part (2004).

Paruch P., Giamarchi T., Triscone J.-M. *Domain wall creep in mixed c-a axis Pb(Zr0.2Ti0.8)O-3 thin films*. Annalen der Physik **13** (1-2): 95-96 (2004).

Rosso A., Giamarchi T. *X-ray spectrum of a pinned charge density wave.* Physical Review B **70** (22): Art. No. 224204 (2004).

Schehr G., Giamarchi T., Le Doussal P. *Specific heat of the quantum Bragg glass*. Europhysics Letters **66** (4): 538-544 (2004).

Ternes M., Weber C., Pivetta M., Patthey F., Pelz J.P., Giamarchi T., Mila F; Schneider W.D. *Scanning-tunneling spectroscopy of surface-state electrons scattered by a slightly disordered two-dimensional dilute "solid": Ce on Ag(111).* Physical Review Letters **93** (14): Art. No. 146805 (2004).

Work made in other institutions

Juricic V.; Benfatto L.; Caldeira A.O., Smith C.M. *Dissipative dynamics of topological defects in frustrated Heisenberg spin systems.* Physical Review B **71** (6): Art. No. 064421 (2005).

Benfatto L., Sharapov S.G., Andrenacci N.; Beck H. *Ward identity and optical conductivity sum rule in the d-density wave state.* Physical Review B **71** (10): Art. No. 104511 (2005).

Benfatto L., Smith C.M. *Optical response for a discrete stripe*. Physica C-Superconductivity and its applications 408-10: 453-454 (2004).

Benfatto L., Sharapov S.G., Beck H. *Effect of orbital currents on the restricted optical conductivity sum rule*. European Physical Journal B **39** (4): 469-473 (2004).

Benfatto L., Toschi A., Caprara S. *Low-energy phase-only action in a superconductor: A comparison with the XY model*. Physical Review B **69** (18): Art. No. 1845 (2004)

Juricic V., Benfatto L., Caldeira A.O., Smith C.M. *Dynamics of topological defects in a spiral: A scenario for the spin-glass phase of cuprates.* Physical Review Letters **92** (13): Art. No. 137202 (2004).

Iucci A., Naon C. *A non-covariant fermionic determinant and its connection to Luttinger systems*. Journal of Physics A- Mathematical and General **38** (3): 749-758 (2005).

Groupe Junod

Bouquet F., Wang Y., Toulemonde P., Guritanu V., Junod A., Eisterer M., Weber H.W., Lee S. and Tajima S. *Using specific heat to scan gaps and anisotropy of MgB_2.* Proceedings of the International Conference on Materials and Mechanisms of Superconductivity and High Temperature Superconductors VII (M^2S-Rio), Rio de Janeiro, Brazil, 25-30 May 2003. Physica C **408-410**, 60-62 (2004).

Guritanu V., Goldacker W., Bouquet F., Wang Y., Lortz R., Goll G. and Junod A. *Specific heat of Nb_3Sn: The case for a second energy gap.* Physical Review B **70** 184526 1-8 (2004).

Uglietti D., Seeber B., Abächerli V., Wang Y.X., Junod A. and Flükiger R. *Critical current, electro-mechanical properties and specific heat of bronze Nb_3Sn conductors.* Proceedings of the Workshop on Accelerator Magnet Superconductors WAMS 2004, 22-24 March 2004, Archamps (France).

Work performed by members of the DPMC in other institutions

Tutsch U., Schweiss P., Wühl H., Obst B., and Wolf Th. *The electronic contribution to the specific heat of $NdBa_2Cu_3O_{6+x}$*. Eur. Phys. J. B **41**,471-478 (2004).

Slebarski A., Grube K., Lortz R., Meingast C. and Löhneisen H.V. *Thermal and magnetic properties of CeRhSn*. J. Magn. Magn. Materials **234-236** (2004) 272-276.

Plackowski T., Sułkowski C., Karpinski J. , Jun J. and Kazakov S.M.. *Magneto-thermopower of single-crystal MgB_2: Evidence for strong electron-phonon coupling anisotropy.* Phys.Rev.B **69** (2004) 104528.

Matusiak M., Plackowski T. and Sulkowski C.. *Correlations between transport coefficients and electronic structure for 1-2-3 ($Ca_{0.1}La_{0.9}$)($Ba_{1.65}La_{0.35}$) Cu_3O_y super-conductors*. Supercond. Sci. Technol. **17** (2004) 596.

Matusiak M., Plackowski T. and Sadowski W.. *The Righi-Leduc effect: on evidence of two-band electronic structure in $Nd_{1.86}Ce_{0.14}CuO_{4-\delta}$.* Solid State Commun. **132** (2004) 24.

Pikul A.P., Kaczorowski D., Bukowski Z., Plackowski T. and Gofryk K.. *Single-crystal study of highly anisotropic $CeNiGe_2$.* J. Phys.: Condensed Matter **16** (2004) 6119.

Groupe van der Marel

Kuzmenko A.B., Tombros N., Mena F.P., Hadipour A., Molegraaf H.J.A., van der Marel D., Grüninger M., and Uchida S. *Redistribution of the c-axis spectral weight and conductivity sum rules in LSCO as revealed by optical transmission*. Physica C 408-410, 300-333 (2004).

van der Marel D. *Expert Opinion, Electrons and bursting waterworks*. Phys. Stat. Sol. (b) **241**, 1391-1392 (2004).

van der Marel D. *Optical spectroscopy of plasmons and excitons in cuprate superconductors*. Journal of Superconductivity: Incorporating Novel Magnetism **17**, 559-577 (2004).

Tsvetkov A.A., Mena F.P., van Loosdrecht P.H.M., van der Marel D., Ren Y., Nugroho A.A., Menovsky A.A., Elfimov I.S. and Sawatzky G.A. *Structural, electronic and magneto-optical properties of YVO3.* Physical Review B **69** 075110 (2004).

Book

van der Marel D. *Optical signatures of electron correlations in the cuprates*. In: "Strong Interactions in Low Dimensions. Seris: Physics and Chemistry of Materials with Low-Dimensional Structures". Vol. 25, D. Baeriswyl, L. Degiorgi (Editors), Kluwer, VI, 441 p., ISBN: 1-4020-1798-7.

Groupe Triscone

Lichtensteiger C. and Triscone J.-M. *Investigation of ferroelectricity in ultrathin $PbTiO_3$ films*. Integrated Ferroelectrics **63**, 143 (2004).

Sarin Kumar A.K., Paruch P., Marré D., Pellegrino L., Tybell T., Ballandras S. and J.-M. Triscone J.-M.. *A novel high frequency surface acoustic wave device based on piezoelectric interdigital transducers.* Integrated Ferroelectrics **63**, 55 (2004).

K. Takahashi K., Matthey D., Jaccard D., Triscone J.-M., Shibuya K., Ohnishi T., and Lippmaa M. *Electrostatic modulation of the electronic properties of Nb-doped $SrTiO_3$ superconducting films*. Applied Physics Letters **84**, 1722 (2004).

Sarin Kumar A.K., Paruch P., Triscone J.-M., Daniau W., Ballandras S., Pellegrino L., Marré D., and Tybell T. *High frequency surface acoustic wave device based on thin film piezoelectric interdigital transducers*. Applied Physics Letter **85**, 1757 (2004).

Lichtensteiger C., Triscone J.-M., Junquera J., and Ghosez P. *Ferroelectricity and tetragonality in ultrathin $PbTiO_3$ films*. Physical Review Letters **94**, 047603 (2005).

Paruch P., Stucki N., Lichtensteiger C., Dawber M., Sarin Kumar A.K., Gariglio S., Matthey M., Takahashi K., and Triscone J.-M. *Nanoscale ferroelectrics.* MaNEP Newsletter Nr. 6 Spring 2004.

Holmes A.T. , Jaccard D., Miyake K. *Signatures of valence fluctuations in $CeCu_2Si_2$ under high pressure.* Physical Review B **69**, 024508 (2004).

Holmes A.T., Jaccard D., Behr G., Inada Y., Onuki Y. *Unconventional superconductivity and non-Fermi liquid behaviour of ε-iron at high pressure*. J. Phys.: Condens. Matter **16**, S1121 (2004).

K. Behnia K., D. Jaccard D., J.J. Flouquet. J.J. *On the thermoelectricity of correlated electrons in the zero-temperature limit.* J. Phys.: Condens. Matter **16**, 5187 (2004).

Wilhelm H., Jaccard D. *Probing the phase diagram of $CeRu_2Ge_2$ by thermopower at high pressure*. Physical Review B **69**, 214408 (2004).

Ph.D. Theses

ABÄCHERLI Vital
Improvement of workability and superconducting properties of high tin content $(Nb,Ta,Ti)_3Sn$ bronze route wires
December 2004

CALVI Marco
Impact of the Mechanical Perturbations on the Performance of the LHC Superconducting Dipole Magnets
December 2004

CUSANELLI Giuseppe
Effects of nano-size powders on microstructure of surface layer of steel obtained by EDM to inhibit nano- and micro-cracks
July 2004

HOLMES Alexander
Exotic Superconducting Mechanisms in Fe and $CeCu_2Si_2$ under Pressure
June 2004

MATTHEY Daniel
Field effects experiments in high-Tc superconductors: a study of the transport properties in the underdoped regime
September 2004

PARUCH Patrycja
Atomic force microscopy studies of ferroelectric domains in epitaxial $PbZr_{0.2}Ti_{0.8}O_3$ thin films and the static and dynamic behavior of ferroelectric domain walls
December 2004

SCHINDL Michael
Préparation et caractéristique de couches biaxiales d'$Yba_2Cu_3O_{7-\delta}$ déposées par pyrolyse d'aérosol sur des rubans d'Argent texturés et des substrats de $SrTiO_3$(100)
July 2004

WANG Yuxing
Specific Heat Study of Unconventional Anisotropic Superconductors: MgB_2, $Yba_2Cu_3O_7$, $NdBa_2Cu_3O_x$
January 2004

Diploma

REYREN Nicolas
Jonctions Josephson à base de NdBa2Cu3O7: Propriétés de Transport sous Champs Magnétique et Electrique
April 2004

RÜETSCHI Anna-Sabina
Etude des effets Nernst, Seebeck et Hall dans des couches minces de $NdBa_2Cu_3O_{6+x}$
April 2004

To be published

Groupe Fischer

Kuffer O., Fischer Ø. *Low temperature growth of pseudocubic perovskites by off-axis rf magnetron sputtering for the realization of epitaxial ferroelectric-based perovskites*, to be published in J. Appl. Phys. **97**, 014103 (2005).

Kugler M., Levy de Castro G., Giannini E., Piriou A., Manuel A.A., Hess C. and Fischer Ø. *First scanning tunnelling spectroscopy on* $Bi_2Sr_2Ca_2Cu_2O_{10+\delta}$. To be published in J. Phys. Chem. Solids (2005).

Kuffer O., Maggio-Aprile I. and Fischer Ø. *Nanoscale ferroelectric field effect writing and reading using scanning tunnelling spectroscopy*. To be published in Nature Mater. (2005).

Fischer Ø., Berthod C., Kugler M., Maggio-Aprile I. and Renner C. *Electron tunneling spectroscopy of high-temperature superconductors*. To be published in Review of Modern Physics, July 2005.

Levy de Castro G., Kugler M., Manuel A.A. and Fischer Ø. *Four-fold structure of vortex core states in* $Bi_2Sr_2CaCu_2O_{8+\delta}$. Submitted to Phys. Rev. Lett. (2004).

Groupe Flükiger

Senatore C., Clayton N., Lezza P., Pace S. and Flükiger R. *Third harmonic susceptibility and Pinning Properties of Fe/*MgB_2 *tapes*. Presented at ASC 04, October 3-8 2004, Jacksonville, Florida. Accepted for publication in IEEE Transactions on Applied Superconductivity.

Seeber B., Uglietti D., Abächerli V., Bovier P.-A., Eckert D., Kübler G., Lezza P., Pollini A. and Flükiger R. *Critical current vs. strain measurement up to 21 T and 1000 A of long length superconducting wires and tapes*. Presented at ASC 04, October 3-8, 2004, Jacksonville, Florida. Accepted for publication in IEEE Transactions on Applied Superconductivity.

Uglietti D., Seeber B., Abächerli V., Banno N. and Flükiger R. *Critical current vs Strain for LTS wires up to 21T*. Presented at ASC 04, October 3-8, 2004, Jacksonville, Florida. Accepted for publication in IEEE Transactions on Applied Superconductivity.

Groupe Giamarchi

Di Ventra M., Berthod C. and Binggeli N. *Heterovalent interlayers and interface states: an ab initio study of GaAs/Si/GaAs(110) and (100) heterostructures*. To appear in Physical Review B [cond-mat/0503283].

Rosso A. and Krauth W. *Variant Monte Carlo algorithm for driven elastic strings in random media.* To be published in J. Comput. Phys.

Groupe van der Marel

Kuzmenko A.B. *KK-constrained variational fitting of optical data*. Rev. Sci. Instr. in press

Mena F.P., van der Marel D., and Sarrao J.L. *Optical conductivity of CeMIns5 (M = Co, Rh, Ir)*. Phys. Rev. B in press.

Mena F.P., Kuzmenko, Hadipour A., van der Marel D., and Babushkina N.A. *Oxygen isotope effect on the optical conductivity of (La0.5Pr0.5)0.7Ca0.3Mn03 thin films.* Phys. Rev. B, in press

Mena F.P., DiTusa J.F., van der Marel D., Aeppli G., Young D.P., Presura C., Damascelli A., Mydosh J.A. *Ferromagnetism makes a doped semiconductor less shiny*. Phys. Rev. Lett. submitted

Groupe Triscone

Paruch P., Giamarchi T., and Triscone J.-M. *Domain wall roughness in epitaxial ferroelectric* $PbZr_{0.2}Ti_{0.8}O_3$ *thin films*. Cond-mat/0412470. To appear in Physical Review Letters.

Jaccard D. and Holmes A.T. *Spin and valence-fluctuation mediated superconductivity in pressurized Fe and* $CeCu_2(Si/Ge)_2$. D. Jaccard , A.T. Holmes. To appear in Physica B

Wilhelm H., Jaccard D., Zlatic V., Monnier R., Delley B., Coqblin B. *High pressure transport properties of* $CeRu_2Ge_2$. To appear in Journal of Physics: Condensed Matter.